Sarm1-Dependent Metabolic Reprogramming of Schwann Cells Following Nerve Injury

Stepanova E.[1,6], Cho, C[1],Lee, J.[1], Pavelec, C.[7,8], Tripathi, A.[1], Vegiraju, T.[1],Hunter-Chang, S.[1,2] , Leitinger, N.[7,8], Campbell , J*[1,2,6], +Deppmann C*[1-6].

[1]Department of Biology, College of Arts and Sciences, Charlottesville, VA 22902
[2]Neuroscience Graduate Program, School of Medicine, University of Virginia, Charlottesville, VA 229022
[3]Department of Biomedical Engineering, School of Engineering, University of Virginia, Charlottesville, VA 22902
[4]Department of Neuroscience, School of Medicine, University of Virginia, Charlottesville, VA 229022
[5]Department of Cell Biology, School of Medicine, University of Virginia, Charlottesville, VA 229022
[6]Program in Fundamental Neuroscience, College of Arts and Sciences, Charlottesville, VA 22902
[7]Department of Pharmacology, School of Medicine, University of Virginia, Charlottesville, VA 229022
[8]Robert M. Berne Cardiovascular Research Center, School of Medicine, University of Virginia, Charlottesville, VA 22902

*To whom correspondence should be sent

Correspondence: jnc4e@virginia.edu, deppmann@virginia.edu

Acknowledgements:
We thank members of the Deppmann, Campbell, and Kucenas labs for helpful discussions. We are grateful to Bogdan Bierowski, Elisabetta Babetto, and Roman Giger for their insightful conversations that contributed to this work. We acknowledge the Keck Center for Cellular Imaging for the use of the Zeiss 780 and 880/980 microscopy systems [PI: AP; NIH-OD025156 and PI: AP; NIH-OD016446]. This research was supported by the NIH National Institute of Neurological Disorders and Stroke (PI: CDD; R01NS091617), American Diabetes Association Pathway to Stop Diabetes (PI: JNC; Award 1-18-INI-14), NIH National Heart, Lung, and Blood Institute (PI: JNC, R01HL153916), and NIH National Eye Institute (PI: JNC, R21EY033528).

Abstract

Schwann cells (SCs) transition into a repair phenotype after peripheral nerve injury, which is crucial for supporting axon regeneration. However, the early SC injury response preceding the repair state remains poorly understood. Here, we demonstrate that Sarm1, a key regulator of axon degeneration, is expressed in SCs and has a critical role in the early SC injury response. Leveraging the fact that Sarm1 deletion impairs the SC transition to the repair state, we used single-nucleus RNA sequencing to compare the transcriptional responses of wild-type and Sarm1 knockout SCs 24 hours after nerve injury. Remarkably, Sarm1-deficient SCs, unlike wild-type SCs, showed increased expression of genes involved in oxidative phosphorylation and the TCA cycle. These findings were functionally validated, revealing that Sarm1 knockout SCs displayed increased mitochondrial respiration in response to injury. Intriguingly, Sarm1 knockout SCs also exhibited enhanced axon protection compared to wild-type SCs in an in vitro model of axon degeneration. We propose that Sarm1 gates the transition of SCs from a protective, oxidative phosphorylation-dependent state (which we term Protection Associated Schwann Cells or PASCs) to a glycolytic, pro-regenerative repair phenotype after injury. Our findings challenge the prevailing view of Sarm1 as an exclusively axon-autonomous regulator of degeneration and reveal a paradigm shift in understanding the role of Sarm1 in the SC injury response, with broad implications for the treatment of peripheral neuropathies and neurodegenerative diseases.

Introduction

Schwann cells (SCs), one of the most numerous cell types of the peripheral nervous system (PNS), play a crucial role in supporting axons and promoting regeneration after injury[1–4]. Following nerve injury, SCs undergo significant changes, transitioning to a repair phenotype characterized by the upregulation of regeneration-associated genes, activation of myelinophagy, and formation of Büngner bands[1,2,5,1,5]. This repair phenotype is driven by the activation of transcription factors, such as c-Jun, which is essential for initiating the SC injury response[6,7].
While the repair SC phenotype is critical for regeneration, this cell state takes time to emerge in mice post-injury[1]. Relatively little work has been done to assess the role of SCs before the emergence of the repair phenotype. Recent findings indicate that immediately following injury, before fully assuming the repair phenotype, SCs adopt a metabolic response crucial for preserving injured axons. This response involves a dramatic glycolytic shift, driven by mTORC1 signaling and associated transcription factors Hif1α and c-Myc, which enhances bioenergetic support to the injured axons, providing essential substrates for maintaining axonal integrity[8]. This early glycolytic shift represents a distinct, proactive role of SCs that precedes their transformation into the repair phenotype. We refer to this post-injury, pre-repair SC state as Protection Associated Schwann Cells (PASCs). Understanding the mechanisms underlying the acquisition and maintenance of the PASC state and its role in axonal preservation could lead to the development of targeted therapies that prevent axonal degeneration, a critical step in improving outcomes after peripheral nerve injury [9,10]. Simultaneously, elucidating the molecular pathways that govern the PASC-to-repair transition could uncover new strategies for enhancing the efficiency of nerve regeneration, thereby promoting better functional recovery [11,12].

Sarm1, a toll-like receptor adaptor protein, has emerged as a central regulator of axonal degeneration[13]. Sarm1 is activated by nicotinamide mononucleotide (NMN), which accumulates in injured axons due to the loss of the NAD+ synthesizing enzyme NMNAT2[14]. Activated Sarm1 cleaves NAD+, leading to a rapid depletion of ATP and subsequent axonal degeneration[15]. Remarkably, genetic deletion of Sarm1 confers robust protection to axons and myelin after injury, preserving their structural integrity and function[13,16,17]. While the vast majority of reports examine the axon-autonomous role of Sarm1, its role in SCs has gone largely unexamined. However, recently it has been demonstrated that Sarm1 is crucial for the timely induction of the SC repair response following peripheral nerve injury[18,19]. In the absence of Sarm1, there is a significant delay in the upregulation of c-Jun in SCs, which is essential for initiating their transformation into a repair phenotype[6]. This is consistent with our previous findings that loss of Sarm1 prevents induction of pJNK in the sciatic nerve 30 minutes after injury[16]. This delay hampers the myelin clearance and regeneration of sensory and motor axons, indicating that Sarm1's role extends beyond its well-documented effects on axonal degeneration[6]. However, a SC-autonomous role for Sarm1 has not been reported. Nevertheless, the requirement of Sarm1 for SC entry into a repair state creates an opportunity to enrich early pre-Repair SC state in Sarm1 knockout (KO) animals to better characterize this novel cell state.
Our study aims to address the following key knowledge gaps: 1. What is the molecular signature and functional role of the early SC injury response, preceding the repair phenotype? 2. How does Sarm1 regulate the transition from PASCs to the repair phenotype? 3. What are the metabolic adaptations associated with the PASC state, and how do they contribute to axonal preservation? To investigate the novel PASC state and its role in the early nerve injury response, we leveraged the Sarm1KO mouse model, which exhibits delayed SC repair program activation, to enrich for PASCs[18,19]. Using single-nucleus RNA sequencing (snRNA-seq), we identified distinct transcriptional profiles of wild-type and Sarm1KO SCs 24 hours after nerve injury. Intriguingly, we found that Sarm1KO SCs were enriched in clusters upregulating genes involved in oxidative phosphorylation and the TCA cycle rather than glycolysis. We then functionally validated these findings and found that Sarm1KO SCs increased mitochondrial respiration after injury. Moreover,

Sarm1KO SCs conferred improved protection against axon degeneration compared to wild-type SCs in an in vitro injury model. Our results suggest that Sarm1 regulates the metabolic reprogramming of SCs after injury, gating their transition from a protective, oxidative phosphorylation-dependent state (PASCs) to a glycolytic, pro-regenerative repair phenotype. This work provides novel insights into the early events of the SC injury response and highlights Sarm1 as a potential therapeutic target for preventing axonal degeneration and optimizing nerve repair.

Results

Sarm1 mRNA expression in Sox10 positive cells

Recent findings have implicated a potential role for Sarm1 in SCs, beyond its well-established axon-autonomous function. It was demonstrated that Sarm1 is crucial for the timely induction of the SC repair response following peripheral nerve injury[18,19]. Moreover, the requirement of Sarm1 for SC entry into a repair state creates an opportunity to study a novel, pre-Repair SC cell state in Sarm1KO animals. However, a previous study reported Sarm1 protein expression in oligodendrocytes but not in SCs of the tibial nerve or dorsal root ganglion, although a low expression of Sarm1 in ~20% of SCs was detected on the PLLn of zebrafish[20]. We examined this by performing Sarm1 and Sox10 RNA fluorescence in situ hybridization (RNA FISH) on WT sciatic nerves (Figure S1.1A-E). We have also detected 20% of Sox10+ cells expressing Sarm1 (Figure S1.1B), with only 0.25 Sarm1 puncta per Sox10+ cell (Figure S1.1C). 3D reconstruction using IMARIS software confirmed Sarm1 RNA puncta localized within SCs (Figure S1.1 E-F). The apparent discrepancy between Sarm1 expression in SCs at the RNA and protein levels may be attributed to differing detection thresholds between in situ hybridization in immunohistochemistry. Given the role of Sarm1 in regulating NAD+ degradation, it is plausible that both Sarm1 mRNA and protein are maintained at extremely low levels in SCs. Our findings confirming Sarm1 RNA expression in SCs open the possibility for a SC-autonomous role for Sarm1 in the injury response.

Single-nucleus RNA sequencing reveals distinct cell populations in WT and Sarm1 knockout mouse sciatic nerves.

Based on our finding that Sarm1 mRNA is expressed in mouse SCs, we hypothesized that Sarm1 might play an active role in these cells. Importantly, recent work has demonstrated that Sarm1 is required for the timely induction of the SC repair program following peripheral nerve injury [18]. This suggests that Sarm1 deficiency may lock SCs into a pre-repair state. To investigate the role of Sarm1 in the SC injury response, we employed single-nuclei RNA-seq (snRNA-seq) on sham and 1 day post-injury sciatic nerves from WT and Sarm1 KO mice (Figure 1A). We surgically transected the right sciatic nerves of male and female 3-6-month-old mice, while the left nerves served as sham controls (Figure 1A). We isolated nuclei from the nerves 1 day post-injury, labeled them for purification by fluorescence-activated cell sorting (FACS) based on nuclei markers (Figure 1A, Figure. S1.2A), followed by cDNA library preparation using 10x Genomics and sequencing. Clustering with Seurat version 5 software [21] based on the top 2000 highly variable genes revealed 11 clusters among 11,544 nuclei from WT and Sarm1KO mice, encompassing both sham and 1-day post-injury samples (Figure 1B). We compared the gene expression profiles of the cell clusters to determine their molecular identities. Our results revealed many canonical cell type marker genes enriched in each cluster, allowing us to identify clusters a1 and a6 as SCs based on their expression of genes such as Mbp, Mpz, Prx, Cadm2, Ncam1 (Figure 1D, Figure S1.2B, Table 1). We annotated other clusters as known cell types based on gene expression profiles reported previously in single-cell RNA sequencing atlases of sciatic nerves[22,23]. The clusters represented various cell types, including endoneurial cells, SCs, perineurial cells, immune cells, epithelial cells, muscle cells, epineurial cells and vascular smooth muscle cells (Figure 1D, Figure S1.2B). We profiled 9,114 nuclei in sham nerves and 2,430 nuclei in injured nerves (Figure 1C). Interestingly, we detected Sarm1 expression in several clusters, including in SC a1 cluster (Figure S1.2H). The proportional composition of different clusters in each genotype for sham and injured (Figure 1E, Figure S1.2C-G) nerves revealed trends in cell number differences between genotype and injury conditions, although only one cluster a4 differed significantly between sham and injured cells, as Sarm1KO samples contributed significantly more cell nuclei to this cluster in response to injury compared to WT counterparts.

SCs in uninjured sciatic nerves of WT and Sarm1KO mice exhibit few differences in gene expression

Before examining the differences between sham and injured SCs between genotypes, we analyzed the transcriptional differences between genotypes in sham sciatic nerves. Selective clustering of sham SCs (Figure 2A-C) revealed four distinct clusters of sham SCs: ss0-ss4 (Figure 2C) with distinct gene expression across every cluster except ss0 (Figure 2D). Cluster ss2 expresses markers characteristic of non-myelinating SCs, such as Cadm2 and Ncam1 [3], while clusters ss0, ss1, ss3 were enriched with myelinating SC markers, such Mbp, Mpz, with ss0 not having specific markers, ss1 being enriched for Erbb4 and Adamtsl4 (Table 2). Ss3 is enriched with calcium signaling (Camk1d), mitochondrial protein synthesis (Cmss1 and Lars2), and lysosomal degradation of glycosphingolipids (Hexb) markers. Cluster ss4 is enriched for markers such as Tshz2, Pdzrn3, Eya2, Zfp521, Tcf4l, suggests that these cells are undergoing transcriptional changes associated with differentiation and maturation, extracellular matrix formation (Col8a1, Fn1), cell adhesion and migration (Smoc2, Scara5), and growth factor signaling modulation (Sulf1) suggesting that these SCs are actively participating in the development and maintenance of the PNS. Interestingly WT and Sarm1KO SCs were unevenly distributed across these clusters (Figure 2E-G), with WT SCs more prevalent in cluster ss0 and Sarm1KO SCs enriched in cluster ss4. Despite some differences between genotypes, we only detected 12 genes differing significantly between WT and Sarm1KO SCs (Figure 2H). Among the 12 genes that differed significantly in expression between WT and Sarm1KO SCs, we saw higher expression of genes such as voltage-gated sodium channel Nav1, Ctnna2 and lower expression of the voltage-gated calcium channel Cacnb4 and histone deacetylase Hdac9 (Figure S2A-C) and little sexual dimorphism in expression of genes like Ctnna2 and Cacnb4 (Figure S2H,I). While sex differences were not prominent, we noted that male SCs differed more between genotypes than did female SCs (Figure S2D-F). Interestingly cluster ss3 is predominantly composed of Sarm1KO female SCs, whereas cluster ss4 is mostly composed of WT female SCs (Figure S2D,E,G). Overall, these results suggest that while minor differences between Sham WT and Sarm1KO SCs are observed, they are minimal, and SCs generally are very similar transcriptionally before injury onset.

SCs exhibit distinct transcriptional profiles in WT and Sarm1 knockout sciatic nerves 1 day after injury

To investigate the differences between WT and Sarm1KO SCs following injury, we selectively re-clustered the SCs from injured nerves (Figure 3A-C). This analysis yielded three clusters of injured nerve SCs: is0, is1, and is2 (Figure 3C). Each cluster exhibited a distinct transcriptional profile (Fig. 3D and Table 3). Some of the top significant genes defining cluster is0 are Rnf208, Reln, and Snap23, while Meg3 expression characterizes cluster is1, and Plp and Fth1 transcripts are prominent in cluster is2. Intriguingly, WT and Sarm1KO injured nuclei were not equally represented across the three clusters (Figure 3E-G). WT nuclei were predominantly present in cluster is0, while Sarm1KO nuclei were more abundant in clusters is1 and is2 (Figure 3E-G). This uneven distribution suggests that while both genotypes respond to injury, they may occupy different transcriptional states along the continuum of the injury response. We postulate that clusters is1 and is2 represent pre-repair SC cell states due to their enrichment with Sarm1KO SCs (Fig. 3E-G). Some sexual dimorphism in cluster representation was also apparent (Figure S3A-C) between genotypes. For example, WT male injured SCs were more heavily represented in cluster is0 compared to female nuclei. In contrast, Sarm1KO female nuclei were more broadly distributed across cluster is0, while male nuclei were more evenly distributed across all three clusters, particularly cluster is1 suggesting that the transcriptional response of male Sarm1 KO SCs to injury deviates further from that of WT SCs compared to their female counterparts.

Sarm1KO SCs upregulate mitochondrial respiration genes required for oxidative phosphorylation 1 day after injury

Our clustering analysis revealed that injury affects WT and Sarm1KO SC gene expression in distinct ways. To investigate these differences, we compared the transcriptional responses of each genotype to injury (Figure 4A, B). Interestingly, WT SCs primarily downregulated genes post-injury, while Sarm1KO SCs predominantly upregulated genes. Among the top differentially regulated genes in WT SCs were Slc1a3, Ptprj, Tgfbi, Pde1c, Ccr5 (upregulated) and Mpz, Qk, Ctnna3, Pmp22, Sema5a (downregulated) (Figure 4A, Table 4). In contrast, Sarm1KO SCs showed upregulation of genes like Snap24, Dscam, Rims2, Kcnb5, Nrg1 and downregulation of Tip2, Cdkn1b, Slc7a2, Arhgap31, Lama2 post-injury (Figure 4B, Table 4).

To gain insights into the functional implications of these transcriptional changes, we performed Gene Ontology (GO) analysis, focusing on KEGG metabolic pathways given the reported importance of SC metabolism in the injury response[8]. Remarkably, among the top 200 differentially regulated genes in WT SCs post-injury, multiple components of the mitochondrial respiration chain were downregulated, including complex I (NADH dehydrogenase), F-type ATPase, cytochrome c oxidase, and TCA cycle enzymes (Figure 4C). In stark contrast, the top 200 differentially regulated genes in Sarm1KO SCs showed upregulation of complex I, F-type ATPase, and cytochrome c oxidase genes post-injury (Figure 4D). Pseudo bulk analysis confirmed the significant downregulation of several mitochondrial respiration genes, such as Ndufb10, Ndufb5, Atp5h, and Cox7c, in Sarm1KO SCs in response to injury (Figure 4E, Figure S4E). Moreover, these genes were enriched in clusters is1 and is2 compared to is0 (Figure 4F, Figure S4F). To validate these findings, we performed in situ hybridization for Ndufb5 and Ndufb10 and observed similar trends to those in the snRNA-seq data (Figure 4G, Figure S4A-D). Quantification of transcript levels in Sox10+ cells revealed a significant decrease in Ndufb5 expression in WT male SCs post-injury, while Sarm1KO cells showed a mild upregulation (Figure S4C). Intriguingly, Ndufb10 expression was significantly upregulated in Sarm1KO male SCs post-injury compared to sham (Figure S4D). Taken together, these results suggest that Sarm1 plays a critical role in regulating the metabolic reprogramming of SCs after injury, potentially promoting a protective phenotype characterized by enhanced mitochondrial respiration in its absence. The opposite regulation of mitochondrial respiration pathways in WT and Sarm1KO SCs highlights the importance of Sarm1 in shaping the SC injury response.

Sarm1 is required for injury-induced shift away from mitochondrial respiration

To functionally validate our snRNA-seq findings, which suggested that WT and Sarm1KO SCs differ in their preferred metabolic pathway after injury, we performed a mitochondrial bioenergetics assay using a Seahorse analyzer. Primary SCs were subjected to a mitochondrial stress test, which included sequential treatment with oligomycin, BAM15, antimycin A, and rotenone, to assess their mitochondrial energetic capacity both basally and under stress. To mimic the effects of injury on SCs in vitro, we activated ErbB2 signaling by adding Neuregulin 1 (Nrg1) for 24 hours, as previously described[8]. Consistent with previous observations[8], Nrg1 treatment did not significantly alter basal, maximal, or ATP-linked oxygen consumption rate (OCR) in WT SCs compared to vehicle control (Figure 5A-C). In contrast, while basal OCR and ATP-linked metabolism remained unchanged in Sarm1KO SCs post-Nrg1 treatment, maximum OCR was significantly increased. This suggests that in the absence of Sarm1, SCs maintain a preference for mitochondrial metabolism even under stress conditions mimicking injury. These data corroborate our snRNA-seq findings and provide functional evidence for the role of Sarm1 in regulating the metabolic reprogramming of SCs after injury. That is, Sarm1 facilitates a transition away from mitochondrial respiration in response to injury.

Sarm1KO SCs confer improved protection against WT axon degeneration in an in vitro injury model

We next sought to investigate whether loss of Sarm1 conferred any improvement on the ability of SCs to improve axon protection after injury. To test this, we established an in vitro microfluidic co-

culture system that allows for the spatial separation of neuronal cell bodies and distal axons[24]. WT superior cervical ganglion (SCG) neurons were cultured and let the axons grow out to the other side of the microfluidic device. Once they did either WT or Sarm1KO SCs were added to the axon side. Following axotomy, achieved by removing the neuronal cell bodies, we assessed the extent of axon degeneration in WT SCG neurons co-cultured with each SC genotype. Surprisingly, WT SCG neurons co-cultured with Sarm1KO SCs exhibited significantly reduced axon degeneration compared to those co-cultured with WT SCs. At 8 hours post-injury, axon degeneration was reduced by 26.8% in the presence of Sarm1KO SCs (Figure 5D,E). These results demonstrate that Sarm1 in SCs contributes to injury-induced axon degeneration *in vitro*, suggesting that it not only gates the metabolic shift from mitochondrial respiration to glycolysis but also regulates the transition of SCs from a protective to a pro-degenerative phenotype.

Discussion

Our findings provide novel insights into the early events of the SC injury response and the mechanisms regulating the transition from a protective to a repair phenotype. We propose that Sarm1 gates the transition of SCs from a protective, oxidative phosphorylation-dependent state, which we term PASCs, to a glycolytic, pro-regenerative repair phenotype. This metabolic reprogramming may be a crucial determinant of SC function after injury, with the PASC state supporting axonal survival and the repair state facilitating debris clearance and regeneration. The identification of PASCs as a distinct functional state of SCs in the early injury response is a significant contribution to our understanding of peripheral nerve degeneration and regeneration.

Importantly, our use of the Sarm1 KO model allowed us to enrich this novel pre-repair SC state. As demonstrated by Giger and colleagues[18], Sarm1 is required for the timely induction of the SC repair program following peripheral nerve injury. This is consistent with the lack of molecular reprogramming toward an SC repair phenotype in Sarm1 KO mice post-injury [19] and the well-characterized lack of phenotypic changes in myelination patterns post-injury in these mutants [13,16,17]. We have also previously shown that Sarm1 is required for induction of p-JNK 30 minutes after sciatic nerve transection [16]. Our snRNA-seq analysis reveals a trend toward decreased expression of c-Jun and Shh in Sarm1KO SCs compared to WT SCs at 24 hpi. Both c-Jun and Shh are critical for the acquisition of the repair Schwann cell phenotype [6,25], and their reduced expression in Sarm1KO SCs further supports the role of Sarm1 in facilitating the timely transition to the repair state following injury. Intriguingly, the Sarm1KO SCs in our study were more protective against axon degeneration than WT SCs (Figure 5D-E). This suggests that the PASCs we identified may represent an even earlier pre-repair state than those previously described [8]. In that study, Bierowski and colleagues concluded that increased aerobic glycolysis and lactate production regulated by Myc, Hif1a, and mTor allowed WT SCs to be protective toward axons. Interestingly, we observed an upregulation of mTOR in Sarm1 KO SCs relative to WT. This is consistent with prior work showing that WT SCs can exert protective effects against the degeneration of enucleated axons in vitro by transporting lactate and pyruvate [8,26]. Given that Sarm1KO SCs conferred enhanced axonal protection compared to WT SCs, we postulate that factors beyond lactate and pyruvate, potentially produced as a result or byproduct of the elevated mitochondrial respiration in PASCs, may contribute to this heightened supportive function.

Our finding on the ability of Sarm1 to regulate cellular metabolism in SCs is consistent with recent work demonstrating that Sarm1 in macrophages regulates cellular metabolism at baseline and after stimulation with inflammatory factors, switching from mitochondrial to non-mitochondrial respiration depending on the trigger [27]. One potential mechanism by which Sarm1 could regulate SC metabolism is through its role as an NADase. NAD+ is a critical cofactor for many metabolic enzymes and has been implicated in the regulation of cellular energy metabolism, redox homeostasis, and cell survival [28,29]. The increased NAD+ levels observed in Sarm1-deficient macrophages [27] and monocytes [30] raise the possibility that Sarm1 may also modulate NAD+ levels in SCs, thereby influencing their metabolic state and function. Given the essential nature of NAD+ in cellular metabolism, especially the electron transport chain, the lack of an NAD+ degrading enzyme (Sarm1) could elevate oxidative phosphorylation preferentially over glycolysis. Furthermore, our observation that components of the complex 1 NADH reductase are upregulated in Sarm1 knockout SCs after injury suggests that NAD+ flux could be a component of this mechanism.

The shift towards oxidative phosphorylation in Sarm1-deficient SCs is intriguing; however, the precise mechanisms by which Sarm1-mediated metabolic changes influence SC function and axonal degeneration and regeneration remain to be fully elucidated. Given the increase in

mitochondrial respiration and the unlikely scenario of elevated lactate production in Sarm1 KO SCs post-injury, alternative protective mechanisms may be at play. One possibility is that the additional ATP generated by oxidative phosphorylation in Sarm1 KO SCs is transported to the axon, providing an energy source that delays axon degeneration. This is supported by evidence showing ATP release from SCs during Wallerian degeneration [31]. Another potential mechanism of enhanced axonal protection by Sarm1 knockout SCs could be through elevated NAD+ levels. It has been demonstrated that NAD+ can be transported from healthy axons into injured axons via gap junctions [32], which could be a plausible mechanism for SC-axon communication. Moreover, elevated NAD+ levels could activate sirtuins such as Sirt2, an NAD+-dependent deacetylase, which has been shown to be transported via exosomes from oligodendrocytes into axons to provide bioenergetic support [33]. Once delivered to the axons, Sirt2 has been shown to elevate ATP levels via deacetylation of Ant1 and Ant2 in axonal mitochondria, boosting mitochondrial ATP production capacity [33].

While the role of Sarm1 has been well established in degenerating axons [13,16,17], it is relatively understudied in non-neuronal cell types. Recent work has established the cell-autonomous presence of Sarm1 in macrophages [27] and monocytes [30]. Giger and colleagues also recently demonstrated that Sarm1 is required for the transition to a repair state, which is essential for proper regeneration [18]; however, they did not determine whether Sarm1 acts SC-autonomously or is working indirectly in other cell types. We demonstrate that Sarm1 mRNA is expressed at low levels in a subset of SCs in the sciatic nerve, which is consistent with previous findings in zebrafish [20]. Furthermore, our in vitro studies show that Sarm1-deficient SCs are capable of slowing down axon degeneration in WT injured axons to a greater extent than wild-type SCs. While these findings are consistent with a SC-autonomous role for Sarm1, further studies using cell type-specific knockout models are necessary to formally demonstrate this concept in vivo.

We propose a working model of SC metabolic reprogramming following axonal injury (Figure 6). In homeostatic conditions, SCs maintain a balanced metabolic profile with no strong preference for either mitochondrial or glycolytic respiration. Upon axonal injury, SCs rapidly transition into PASCs, characterized by upregulated mitochondrial respiration. This metabolic state appears to correspond with axonal protection, potentially by providing energy-rich metabolites to compromised axons. Subsequently, Sarm1 activation triggers a metabolic shift in SCs towards increased glycolysis and lactate production, concurrent with reduced mitochondrial respiration. This later metabolic state likely supports the transition from axon preservation to regeneration, facilitating debris clearance and providing metabolic substrates conducive to axon regrowth. This model highlights the critical role of Sarm1 in orchestrating the metabolic plasticity of SCs, thereby regulating the balance between axon protection and regeneration in response to injury.

Our findings have important clinical implications for the treatment of peripheral nerve injuries and neurodegenerative conditions. By identifying Sarm1 as a key regulator of SC metabolism and function, we highlight a potential therapeutic target for preventing axonal degeneration and enhancing nerve regeneration. Inhibiting Sarm1 activity in SCs early after injury could prolong the PASC state, providing a window of opportunity for axonal preservation without the need to degenerate the axon [34]. However, the timing of intervention will be critical, as prolonged Sarm1 inhibition could impair the transition to the repair state and hinder regeneration. Therefore, future studies should focus on elucidating the optimal therapeutic window for Sarm1 modulation and exploring combinatorial approaches that target multiple aspects of the SC injury response.

Our study also raises several intriguing questions for future research. First, the precise molecular mechanisms by which Sarm1 regulates SC metabolism and the transition from PASCs to repair SCs need to be elucidated. This could involve investigating the interplay between Sarm1, NAD+

metabolism, and key transcriptional regulators such as c-Jun, c-Myc, and Hif1α. Second, the potential role of Sarm1 in modulating SC-axon metabolic coupling warrants further investigation. This could include examining the transfer of metabolites or signaling molecules between SCs and axons in the presence and absence of Sarm1. Third, the long-term consequences of prolonging the PASC state on axonal health and regeneration capacity should be explored. This could involve developing methods to reversibly modulate Sarm1 activity in SCs and assessing the impact on nerve repair outcomes.

In conclusion, our study reveals a novel role for Sarm1 in regulating SC metabolism and function following peripheral nerve injury. By integrating our findings with recent work on the role of Sarm1 in macrophage metabolism [27] and the broader SC injury response [18], we provide a more comprehensive understanding of how Sarm1 coordinates the cellular and molecular events that underlie successful nerve repair and regeneration. Our results highlight the complex interplay between glial cell metabolism, neuronal survival, and axonal regeneration, and underscore the importance of considering these factors in the development of new therapies for peripheral nerve injuries and related disorders. Future studies should aim to map the detailed timeline of SC injury response using high-resolution approaches, investigate Sarm1's role in other glial cells like oligodendrocytes, and translate these findings to human SCs and peripheral nerve injuries to develop targeted therapies.

Methods

EXPERIMENTAL MODEL AND STUDY PARTICIPANT DETAILS

Animals

Mice: All animal care and experiments were performed in compliance with the Association for Assessment of Laboratory Animal Care policies and approved by the University of Virginia Animal Care and Use Committee. All mice are on a C57BL/6J.129S mixed background. C57BL/6J (referred to as WT) and Sarm1 knockout (referred to as Sarm1KO) animals were purchased from Jackson Labs. All snRNA-seq experiments were carried out in adult (3-6 month old) mice.

In Vitro Experiments

Superior Cervical Ganglia (SCG) Culture: Mouse pups aged P1-P2 were dissected to isolate superior cervical ganglia (SCG). SCGs were plated at a density of 1 SCG in each compartmentalized microfluidic device (MFD) as described earlier (Deppmann et al. 2008). Neurons were cultured in DMEM supplemented with 10% FBS, penicillin/streptomycin (1 U/mL), and 45 ng/mL of NGF derived from mouse salivary glands. Contaminating glia were removed using 10 µM cytosine arabinofuranoside (Sigma-Aldrich, catalog 10931) for 48 hours. Cultures were maintained until days 5-7 and used only if they had successfully extended axon projections to the opposing side of the MFD.

SC Culture: Mouse pups aged P1-P3 were dissected to isolate sciatic nerves. SC isolation and culture were performed as described earlier [35] with some modifications. Sciatic nerves were isolated and enzymatically digested in 0.05% Type I Collagenase (Worthington Biochemical Corp, catalog LS004196) for 30 minutes, followed by 30 minutes in 0.125% Trypsin (Millipore T4799-5G). Nerves were further mechanically dissociated by trituration. After centrifugation at 300 xg for 5 minutes, cells were purified using a 70 µm filter (Corning, catalog 352350) and plated at about 30,000 cells/cm^2. Cells were cultured in MEM supplemented with heat-inactivated Normal Horse Serum (Invitrogen, catalog 26050088) and 1:100 Pen-Strep (Gibco, catalog 15070-063), 2 µM Forskolin (Sigma, catalog F3917), and 10 µM Neuregulin (PeproTech, catalog 100-03). The next day, the media was changed and supplemented with 10 µM cytosine arabinofuranoside (Sigma-Aldrich, catalog 10931) for 24 hours, as described earlier, to help remove proliferating fibroblasts [36]. After that, cytosine arabinofuranoside was removed, and cells were maintained for up to a week until ready for experiments.

SCG-SC Co-Culture: 4-5 days after SCG plating, Schwann cells were removed from the dish using 0.05% Trypsin-EDTA and plated into the distal axon side of SCG MFDs at 10,000 cells/MFD. Cells were allowed to establish connections with axons for 1 day. Then, the cell body side of microfluidic devices was aspirated as described earlier [24]. 8 hours post-injury, cells were fixed in 4% paraformaldehyde for 20 minutes, washed 3 times in PBS, blocked in 5% donkey serum, 0.05% Triton-X-100 in PBS for 1 hour at room temperature. This was followed by primary antibody staining overnight at 4°C (Tuj1 (1:1000, made on site) and Sox10 (1:150, ThermoFisher, catalog PA5-37890). The next day, cells were washed 3 times in PBS, followed by a 1-hour incubation in Donkey anti-Mouse Alexa Fluor 568 (Fisher, catalog A10037) and Donkey anti-goat Alexa Fluor 488, then washed 3 more times in PBS. Mounting medium with Dapi Fluoromount-G (SouthernBiotech, catalog OB010020) was applied. Cells were imaged on a Zeiss LSM 780 confocal microscope in the W. M. Keck Center at the University of Virginia.

METHOD DETAILS

Sciatic Nerve Transection Surgeries

Mice were anesthetized with isoflurane, and eye lubrication was provided. Fur was removed from the right side of the back/hindlimb region, and the area was cleaned with 3 alternating wipes of iodine and 70% alcohol. Prior to incision, bupivacaine was applied locally (0.001 mL/gram mouse body weight, 0.25% solution) to prevent pain at the surgery site. An incision was made through the skin over the dorsal hindlimb region. Blunt dissection through the muscle allowed access to the sciatic nerve, which was transected with a pair of sterile surgical scissors, and a 2mm nerve segment was removed. The gluteal muscles were then brought back into their original anatomical position and secured in place with surgical sutures, and the skin was reapproximated by surgical sutures. The animal was also administered ketoprofen for pain management (0.004 mL/gram mouse body weight, 1 mg/mL concentration).

Tissue Harvest

One day after surgery, mice were rapidly cervically dislocated without anesthesia for tissue collection to avoid confounding factors of anesthesia or CO_2 on the rapidly changing transcriptome of the already injured sciatic nerve. Uninjured (sham) and injured sciatic nerves were immediately collected, avoiding a 2 mm stump at the injury site, and uninjured or sham nerves (left side) were collected. Visual confirmation that surgery yielded transection (rather than crush) and that the ends did not rejoin was also performed prior to harvest. Distal to cell body sciatic nerves were collected, placed in a vial, and immediately flash-frozen in liquid nitrogen. Tissue was stored at -80 °C until further processing.

Nuclei Isolation, Library Preparation, and Sequencing

Tissue was defrosted, and 4-6 nerves per condition were pooled. There were a total of 8 different conditions: WT and Sarm1KO male and female nerves, each split into sham and injury groups. Pooled nerves from each condition were dounce homogenized, and nuclei were purified by density gradient centrifugation as described earlier [37,38] and re-suspended in resuspension buffer (molecular-grade PBS with 1% BSA, 0.1% Protector RNase inhibitor, 2mM $MgCl_2$). Following that, Total Seq anti-Nuclear Pore Complex Proteins Hashtags (BioLegend, catalog numbers: 682209, 682211, 682213, 682205, 682207, 682215, 682219) were applied to track the sample from which nuclei originated before pooling. Samples then received NucBlue stain (Invitrogen, catalog R37605), and batches 4 and 5 were also stained with Donkey anti-Mouse IgG (H+L) Highly Cross-Adsorbed Secondary Antibody, Alexa Fluor 647 (ThermoFisher, catalog A-31571, 1:100) that binds to Total Seq antibodies to increase the purity of the nuclear fraction. The first batch was sorted on a Sony SH800 Cell Sorter, while the rest were sorted based on NucBlue+/AlexaFluor647+ nuclei on a Becton Dickinson Influx cell sorter. To ensure a clear fraction, we first gated based on a highly fluorescent Alexa Fluor 647 signal (Supplemental Figure 1A), followed by selecting cells of appropriate size and complexity using forward vs. side scatter distribution. We then ensured that only singlets were selected by plotting trigger pulse width vs. forward scatter. Lastly, we selected a DNA intercalator with a highly fluorescent fraction. With these settings, nuclei were sorted in 18.8 µL of RT Reagent B from the 10x Genomics Chromium Next GEM Single Cell 3' Kit v3.1. The remaining components of the Step 1 master mix reagents were combined in the capture tube, along with sufficient resuspension buffer to achieve a total volume of 75 µL. Subsequently, we followed the manufacturer's instructions (10X Genomics, CG000204 Rev D) to process the sample into complementary DNA (cDNA) sequencing libraries. For the hashtag oligonucleotide (HTO) libraries, we followed a previously published protocol [39], with a modification: double-sided SPRI (solid-phase reversible immobilization) was performed twice to effectively separate HTO libraries from cDNA libraries after amplification and, if necessary, just before pooling libraries for sequencing. The first 3 batch libraries were then sequenced on the Illumina NextSeq 550 using a 75-cycle, high-output kit, while the last 2 batches

were sequenced with NextSeq 2000 using a P2 100-cycle run following the manufacturer's instructions.

Data Analysis of Sequencing Data

We used the 10X Genomics Cell Ranger pipeline (version 5.0) to align reads to the mouse reference transcriptome (mm10-2020-A) and calculate gene-level expression values with Unique Molecular Identifier (UMI) correction. The inclusion of introns was enabled using the Cell Ranger include-introns parameter. Hashtag (further referred to as hashtag oligonucleotide, HTO) demultiplexing was performed using a pipeline published previously [40]. We implemented filters for each library based on their distribution of quality metrics (see code for specifics). Libraries with HTOs underwent filtering, where cells that expressed multiple HTOs (doublets) or no HTOs (no binding occurred or non-nuclear RNA) were eliminated from the analysis. Subsequently, all 5 batches were integrated to correct for technical variance[41]. We then log-normalized the data, selected the top 2,000 highest variance genes, integrated the libraries in Seurat, scaled the data, conducted Principal Component Analysis (PCA) to reduce the dimensionality of the high-variance gene space, and clustered the cells using the Louvain algorithm based on Euclidean distance in the PCA space. Non-linear dimensionality reduction was performed through Uniform Manifold Approximation and Projection [42] for visualizing the clustered data in two dimensions. To select the most variable genes between genotypes and conditions, we employed the Edge Libra Differential Expression in R, which averages cells by batch within each cluster into a pseudo-bulk sample before performing differential expression analysis [43].

RNA Fluorescence In Situ Hybridization (RNA FISH) Procedure

RNA FISH experiments were performed on sciatic nerves obtained as described in the "Tissue Harvest" section. However, the tissue was fresh frozen in Tissue-Tek® O.C.T. Compound (Sakura, catalog 4583) submerged in liquid nitrogen, cryo-sectioned on a cryostat (Thermo Scientific, Microm HM 525) at 10 µm thickness, and stored at -80 °C until ready to use. On the day before RNA FISH, slides were brought to room temperature and immediately incubated in 10% formalin for 20 minutes. They were then washed 3 times in PBS and left to dry overnight. The next day, sections underwent incubation for 10 minutes in hydrogen peroxide at room temperature, followed by Protease IV in a HybEZ II Oven at 40 °C. The tissue was then exposed to a 2 hour incubation with the probe of interest (Ndufb5, Ndufb10, Sox10, or Sarm1) at 40 °C. The tissue further underwent treatments with AMP1, 2, and 3, followed by HRP-C1, C2, C3, and HRP Blocker, components of (ACD Bio catalogs 323110, 322381). The fluorophores used to visualize probes of interest were TSA Plus FITC, Cy3, and Cy5 (Akoya Biosciences, catalog numbers NEL741001KT, NEL744001KT, NEL745001KT). Slides with tissue were covered with mounting medium DAPI Fluoromount-G (Fisher/SouthernBiotech, catalog OB010020) and coverslipped. Z-stack images were captured using a Leica Stellaris 5, and Zeiss 980 with a Z interval of 0.5 µm and the number of Z stacks being determined empirically for each image.

Image Analysis

RNA FISH:

To analyze the images, the Z-stacks were compressed using maximum intensity projection into a single plane image and imported into QuPath software. A mask over DAPI-positive nuclei was automatically selected to measure expression of transcripts in nuclei. To measure total cell expression, a 5 µm expansion around the nucleus was drawn automatically by the software to predict cytoplasm boundaries. The software was trained by a set of images selected by a blinded investigator to identify nuclei and cells positive for Sox10 probe (ACD, catalog 435931-C3) signal. The software was further trained to identify other probes (Ndufb5 (ACD, catalog 1303021-C1), Ndufb10 (ACD, catalog 1303041-C2), Ctnna2 (ACD, catalog 1303031-C2), and Sarm1 (ACD,

catalog 504191-C2)). Eventually, the percentage of Sox10-positive cells also positive for probes of interest was quantified and compared between conditions using mean +/- standard error of the mean (SEM) and analyzed using unpaired t-test.

Immunocytochemistry:

A blinded investigator quantified axon degeneration from fluorescence microscope images of cultured, Tuj1-immunostained axons as described earlier [16,24,44]. In brief, randomly assigned 50 µm lines tracing along the length of axons, avoiding bundled axons. The investigator then counted the number of boxes containing 3 or more beads/blebs, categorizing them as degenerating axons. The percentage of total degenerating axons was calculated using Microsoft Excel. Data were represented as mean +/- standard error of the mean (SEM), two-way ANOVA with Turkey multiple comparisons test was performed to analyze differences between conditions. Each experiment was conducted a minimum of 3 times using separate litters of mouse pups as a separate replicate.

Mitochondrial Stress Test

SCs were isolated from WT and Sarm1KO P0-P21 sciatic nerves and plated at 20,000 cells/well of an XFe96 cell culture microplate for 5-7 days as described above, with one difference: SCs were supplemented with 20 µg/mL of Bovine Pituitary Extract (Fisher Scientific, catalog 13-028-014) instead of Nrg. 24 hours before the assay, a set of wells was subjected to Nrg treatment (200 ng/ml), simulating injury. After Nrg treatment, the media was changed to mitochondrial stress test medium (Corning catalog 50-003-PB). Mitochondrial activity was assessed by measurement of O_2 consumption rate on a Seahorse XFe96 instrument (Agilent Technologies). The rate of O_2 change was measured every 13 minutes for a 3-minute interval before sequential challenge with 1) 1 µM oligomycin (Sigma Aldrich catalog 75351), 2) 2 µM BAM15 (Cayman Chemical Company catalog 17811), and 3) 10 µM antimycin A (Sigma-Aldrich catalog A8674) and 10 µM rotenone (Sigma-Aldrich catalog R88751G). Maximal OCR was measured as post-BAM15 OCR minus post-antimycin A/rotenone OCR. Basal OCR was measured as pre-oligomycin OCR minus post-antimycin A/rotenone OCR. Upon completion of the assay, cells were immediately fixed in 4% PFA for 20 minutes, washed 3x in PBS for 5 minutes and incubated in a DAPI mounting medium. Cells were imaged on a Zeiss LSM 780 confocal microscope in the W. M. Keck Center at the University of Virginia, cell quantification was performed using QuPath software. The values from mitochondrial activity measurements were normalized to cell numbers in each well. Data is represented as mean +/- standard error of the mean (SEM) with each data point representative of independent litters harvested, unpaired two-tailed t-tests were used to analyze differences between conditions.

QUANTIFICATION AND STATISTICAL ANALYSIS

Quantifications and statistical analysis were performed for different assays as described in methods and legends.

Lead Contact

Further information and requests for resources and reagents should be directed to and will be fulfilled by the lead contact, Christopher Deppmann, Ph.D. (deppmann@virginia.edu) and John Campbell, PhD (jnc4e@virginia.edu).

Author contributions

E.S., J.C., N.L., and C.D. planned all the experiments. E.S., C.C., J.L, C.P., A.T., T.V., S.H-C performed all the experiments and analyzed the data. E.S., C.D., J.C. wrote the manuscript with contributions from co-authors

Declaration of generative AI and AI-assisted technologies in the writing process: During the preparation of this work the authors used Anthropic for proofing and grammar. After using this tool/service, the authors reviewed and edited the content as needed and takes full responsibility for the content of the publication.

Declaration of competing interests: The authors declare no competing interests.

Bibliography

1. Jessen KR, Mirsky R. The repair Schwann cell and its function in regenerating nerves. J Physiol (Lond) 2016; 594:3521–31.
2. Jessen KR, Arthur-Farraj P. Repair Schwann cell update: Adaptive reprogramming, EMT, and stemness in regenerating nerves. Glia 2019; 67:421–37.
3. Jessen KR, Mirsky R. The success and failure of the schwann cell response to nerve injury. Front Cell Neurosci 2019; 13:33.
4. Cattin A-L, Lloyd AC. The multicellular complexity of peripheral nerve regeneration. Curr Opin Neurobiol 2016; 39:38–46.
5. Gomez-Sanchez JA, Carty L, Iruarrizaga-Lejarreta M, Palomo-Irigoyen M, Varela-Rey M, Griffith M, Hantke J, Macias-Camara N, Azkargorta M, Aurrekoetxea I, et al. Schwann cell autophagy, myelinophagy, initiates myelin clearance from injured nerves. J Cell Biol 2015; 210:153–68.
6. Arthur-Farraj PJ, Latouche M, Wilton DK, Quintes S, Chabrol E, Banerjee A, Woodhoo A, Jenkins B, Rahman M, Turmaine M, et al. c-Jun reprograms Schwann cells of injured nerves to generate a repair cell essential for regeneration. Neuron 2012; 75:633–47.
7. Gomez-Sanchez JA, Pilch KS, van der Lans M, Fazal SV, Benito C, Wagstaff LJ, Mirsky R, Jessen KR. After nerve injury, lineage tracing shows that myelin and remak schwann cells elongate extensively and branch to form repair schwann cells, which shorten radically on remyelination. J Neurosci 2017; 37:9086–99.
8. Babetto E, Wong KM, Beirowski B. A glycolytic shift in Schwann cells supports injured axons. Nat Neurosci 2020; 23:1215–28.
9. Conforti L, Gilley J, Coleman MP. Wallerian degeneration: an emerging axon death pathway linking injury and disease. Nat Rev Neurosci 2014; 15:394–409.
10. Cashman CR, Höke A. Mechanisms of distal axonal degeneration in peripheral neuropathies. Neurosci Lett 2015; 596:33–50.
11. Scheib J, Höke A. Advances in peripheral nerve regeneration. Nat Rev Neurol 2013; 9:668–76.
12. Gordon T, English AW. Strategies to promote peripheral nerve regeneration: electrical stimulation and/or exercise. Eur J Neurosci 2016; 43:336–50.
13. Osterloh JM, Yang J, Rooney TM, Fox AN, Adalbert R, Powell EH, Sheehan AE, Avery

MA, Hackett R, Logan MA, et al. dSarm/Sarm1 is required for activation of an injury-induced axon death pathway. Science 2012; 337:481–4.

14. Figley MD, Gu W, Nanson JD, Shi Y, Sasaki Y, Cunnea K, Malde AK, Jia X, Luo Z, Saikot FK, et al. SARM1 is a metabolic sensor activated by an increased NMN/NAD+ ratio to trigger axon degeneration. Neuron 2021; 109:1118-1136.e11.

15. Gerdts J, Brace EJ, Sasaki Y, DiAntonio A, Milbrandt J. SARM1 activation triggers axon degeneration locally via NAD^+ destruction. Science 2015; 348:453–7.

16. Gamage KK, Cheng I, Park RE, Karim MS, Edamura K, Hughes C, Spano AJ, Erisir A, Deppmann CD. Death Receptor 6 Promotes Wallerian Degeneration in Peripheral Axons - supplementals. Current Biology 2017; 27:890–6.

17. Gerdts J, Summers DW, Sasaki Y, DiAntonio A, Milbrandt J. Sarm1-mediated axon degeneration requires both SAM and TIR interactions. J Neurosci 2013; 33:13569–80.

18. Schmitd LB, Hafner H, Ward A, Asghari Adib E, Biscola NP, Kohen R, Patel M, Williamson RE, Desai E, Bennett J, et al. Sarm1 is not necessary for activation of neuron-intrinsic growth programs yet required for the Schwann cell repair response and peripheral nerve regeneration. BioRxiv 2024;

19. Tian W, Czopka T, López-Schier H. Systemic loss of Sarm1 protects Schwann cells from chemotoxicity by delaying axon degeneration. Commun Biol 2020; 3:49.

20. Fazal SV, Mutschler C, Chen CZ, Turmaine M, Chen C-Y, Hsueh Y-P, Ibañez-Grau A, Loreto A, Casillas-Bajo A, Cabedo H, et al. SARM1 detection in myelinating glia: sarm1/Sarm1 is dispensable for PNS and CNS myelination in zebrafish and mice. Front Cell Neurosci 2023; 17:1158388.

21. Hao Y, Stuart T, Kowalski MH, Choudhary S, Hoffman P, Hartman A, Srivastava A, Molla G, Madad S, Fernandez-Granda C, et al. Dictionary learning for integrative, multimodal and scalable single-cell analysis. Nat Biotechnol 2024; 42:293–304.

22. Gerber D, Pereira JA, Gerber J, Tan G, Dimitrieva S, Yángüez E, Suter U. Transcriptional profiling of mouse peripheral nerves to the single-cell level to build a sciatic nerve ATlas (SNAT). eLife 2021; 10.

23. Zhao X-F, Huffman LD, Hafner H, Athaiya M, Finneran MC, Kalinski AL, Kohen R, Flynn C, Passino R, Johnson CN, et al. The injured sciatic nerve atlas (iSNAT), insights into the cellular and molecular basis of neural tissue degeneration and regeneration. eLife 2022; 11.

24. Yong Y, Hughes C, Deppmann C. A microfluidic culture platform to assess axon degeneration. Methods Mol Biol 2020; 2143:83–96.

25. Ramesh R, Manurung Y, Ma KH, Blakely T, Won S, Moreno-Ramos OA, Wyatt E, Awatramani R, Svaren J. JUN Regulation of Injury-Induced Enhancers in Schwann Cells. J Neurosci 2022; 42:6506–17.

26. Mutschler C, Fazal SV, Schumacher N, Loreto A, Coleman MP, Arthur-Farraj P. Schwann cells are axo-protective after injury irrespective of myelination status in mouse Schwann

cell-neuron cocultures. J Cell Sci 2023; 136.

27. Shanahan KA, Davis GM, Doran CG, Sugisawa R, Davey GP, Bowie AG. SARM1 regulates NAD+-linked metabolism and select immune genes in macrophages. J Biol Chem 2024; 300:105620.

28. Houtkooper RH, Cantó C, Wanders RJ, Auwerx J. The secret life of NAD+: an old metabolite controlling new metabolic signaling pathways. Endocr Rev 2010; 31:194–223.

29. Koch-Nolte F, Fischer S, Haag F, Ziegler M. Compartmentation of NAD+-dependent signalling. FEBS Lett 2011; 585:1651–6.

30. Sugisawa R, Shanahan KA, Davis GM, Davey GP, Bowie AG. SARM1 regulates pro-inflammatory cytokine expression in human monocytes by NADase-dependent and -independent mechanisms. iScience 2024; 27:109940.

31. Shin YH, Lee SJ, Jung J. Secretion of ATP from Schwann cells through lysosomal exocytosis during Wallerian degeneration. Biochem Biophys Res Commun 2012; 429:163–7.

32. Zhao YJ, Zhu WJ, Liu J, Li WH, Zhao ZY, Huang C, Yang JY, Lee HC. Gap junction intercellular communications regulates activation of SARM1 and protects against axonal degeneration. Res Sq 2024;

33. Chamberlain KA, Huang N, Xie Y, LiCausi F, Li S, Li Y, Sheng Z-H. Oligodendrocytes enhance axonal energy metabolism by deacetylation of mitochondrial proteins through transcellular delivery of SIRT2. Neuron 2021; 109:3456-3472.e8.

34. Abay ZC, Wong MY-Y, Teoh J-S, Vijayaraghavan T, Hilliard MA, Neumann B. Phosphatidylserine save-me signals drive functional recovery of severed axons in Caenorhabditis elegans. Proc Natl Acad Sci USA 2017; 114:E10196–205.

35. Andersen ND, Monje PV. Isolation, Culture, and Cryopreservation of Adult Rodent Schwann Cells Derived from Immediately Dissociated Teased Fibers. Methods Mol Biol 2018; 1739:49–66.

36. Wei Y, Zhou J, Zheng Z, Wang A, Ao Q, Gong Y, Zhang X. An improved method for isolating Schwann cells from postnatal rat sciatic nerves. Cell Tissue Res 2009; 337:361–9.

37. Habib N, Li Y, Heidenreich M, Swiech L, Avraham-Davidi I, Trombetta JJ, Hession C, Zhang F, Regev A. Div-Seq: Single-nucleus RNA-Seq reveals dynamics of rare adult newborn neurons. Science 2016; 353:925–8.

38. Todd WD, Venner A, Anaclet C, Broadhurst RY, De Luca R, Bandaru SS, Issokson L, Hablitz LM, Cravetchi O, Arrigoni E, et al. Suprachiasmatic VIP neurons are required for normal circadian rhythmicity and comprised of molecularly distinct subpopulations. Nat Commun 2020; 11:4410.

39. Gaublomme JT, Li B, McCabe C, Knecht A, Yang Y, Drokhlyansky E, Van Wittenberghe N, Waldman J, Dionne D, Nguyen L, et al. Nuclei multiplexing with barcoded antibodies for single-nucleus genomics. Nat Commun 2019; 10:2907.

40. Stoeckius M, Zheng S, Houck-Loomis B, Hao S, Yeung BZ, Mauck WM, Smibert P, Satija R. Cell Hashing with barcoded antibodies enables multiplexing and doublet detection for single cell genomics. Genome Biol 2018; 19:224.

41. Hao Y, Hao S, Andersen-Nissen E, Mauck WM, Zheng S, Butler A, Lee MJ, Wilk AJ, Darby C, Zager M, et al. Integrated analysis of multimodal single-cell data. Cell 2021; 184:3573-3587.

42. McInnes L, Healy J. UMAP: Uniform Manifold Approximation and Projection for Dimension Reduction. arXiv.org 2018;

43. Squair JW, Gautier M, Kathe C, Anderson MA, James ND, Hutson TH, Hudelle R, Qaiser T, Matson KJE, Barraud Q, et al. Confronting false discoveries in single-cell differential expression. Nat Commun 2021; 12:5692.

44. Yong Y, Gamage K, Cheng I, Barford K, Spano A, Winckler B, Deppmann C. p75NTR and DR6 Regulate Distinct Phases of Axon Degeneration Demarcated by Spheroid Rupture. J Neurosci 2019; 39:9503–20.

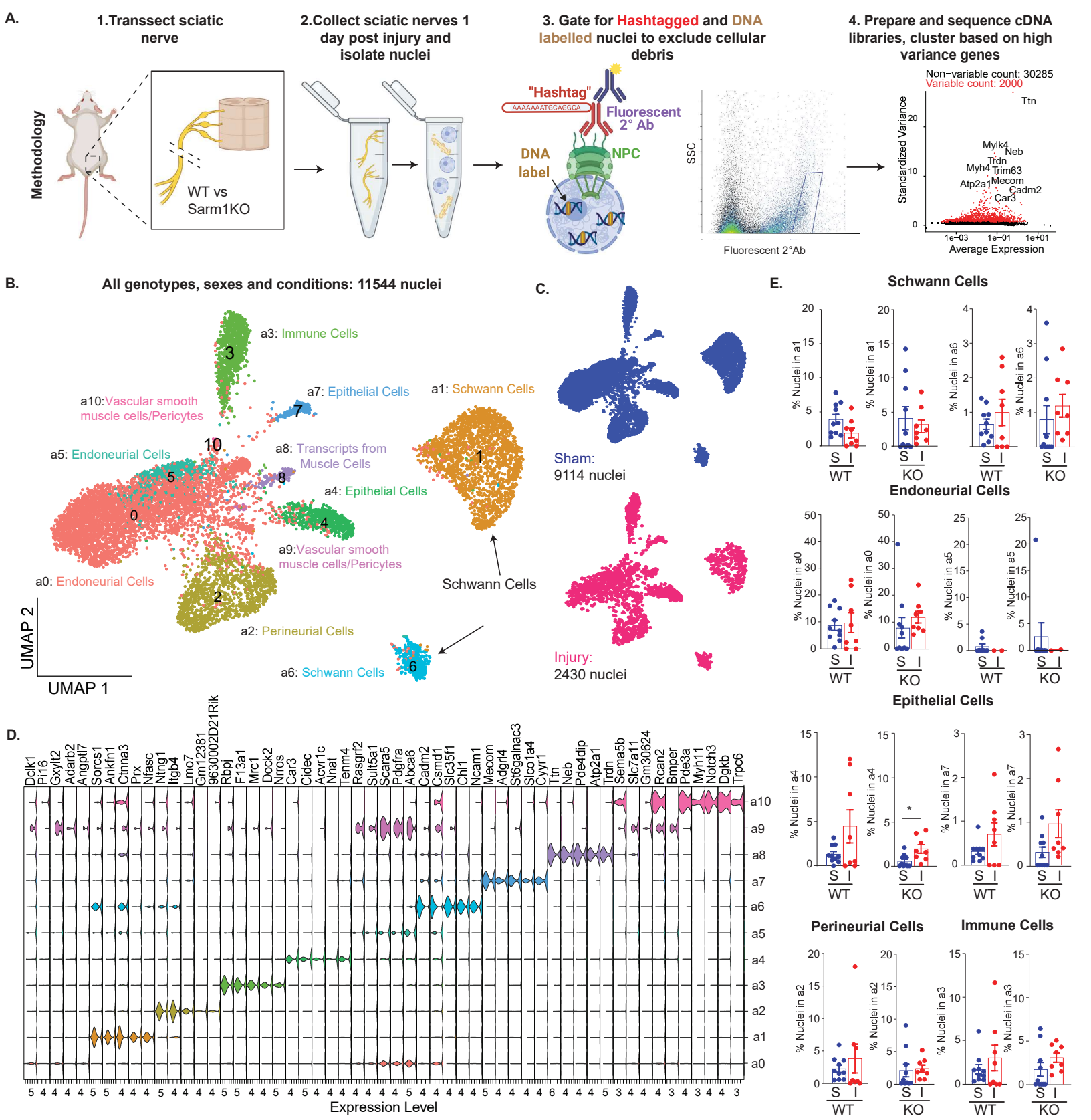

Figure 1. Overview of single nucleus RNA Sequencing (sn-RNA-seq) in mouse WT and Sarm1KO sciatic nerves.

FIGURE LEGENDS

Figure 1: Overview of single-nucleus RNA Sequencing (snRNA-seq) in WT and Sarm1KO mouse sciatic nerves. A. Schematic workflow of the snRNA-seq protocol: 1) Surgical transection of right sciatic nerve; left sciatic nerve used as sham control; 2) Nerve collection 1 day post-surgery; nuclei isolation via dounce homogenization and density-gradient purification; 3) FACS purification of nuclei using DNA-barcoded antibodies against Nuclear Pore Complex (NPC) and DNA intercalator counterstain; 4) cDNA library preparation, sequencing, and data analysis. **B.** UMAP plot displaying clusters of single-nucleus transcriptomes from sham and injured sciatic nerves of wildtype (WT) and Sarm1KO mice, including both male and female samples. **C.** Split UMAP plots showing distribution of nuclei from sham (left) and injured (right) conditions. **D.** Violin plots depicting relative expression levels of marker genes for each identified cluster. **E.** Bar plots representing the percentage of nuclei in each cluster for Schwann Cells, Endoneurial Cells, Epithelial Cells, Perineurial Cells, and Immune Cells across different conditions. Each dot represents a batch that includes multiple biological replicates. Percentages were calculated by dividing the number of cells in a specific cluster by the total number of cells for each biological replicate (e.g., Schwann Cells in cluster a1 for WT Sham mice). Data presented as mean ± standard error of the mean (SEM). * indicates $p = 0.0133$. S = Sham, I = Injury.

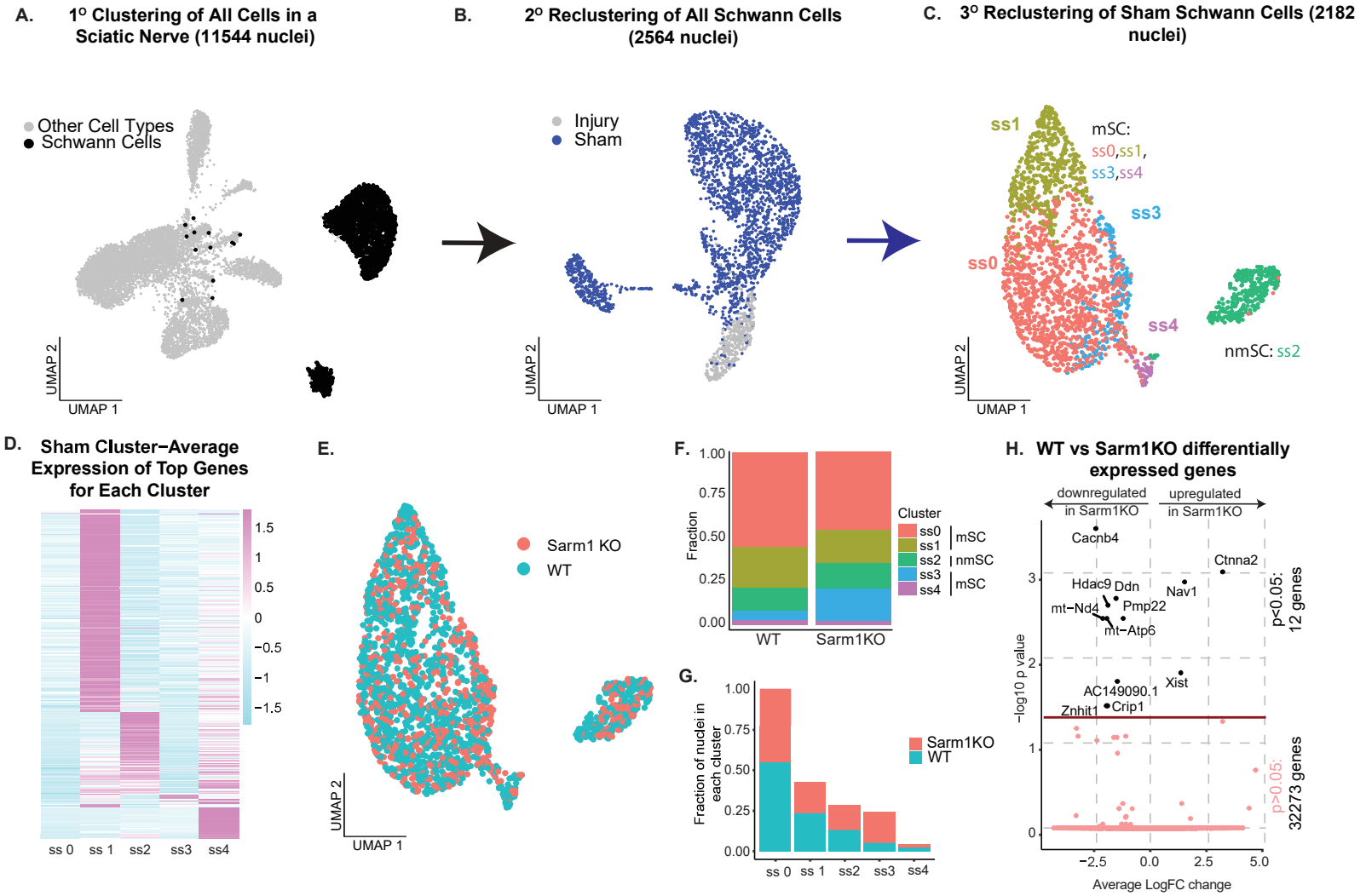

Figure 2. Schwann Cells in uninjured sciatic nerves of WT and Sarm1KO mice exhibit few differences in gene expression

Figure 2: Schwann Cells in uninjured sciatic nerves of WT and Sarm1KO mice exhibit minimal differences in gene expression. A. UMAP showing selection of Schwann Cell (SC) clusters a1 and a6 (highlighted in black) for reclustering. **B.** UMAP of secondary clustering analysis performed exclusively on SCs. **C.** UMAP of tertiary clustering analysis on SCs from uninjured nerves (Sham SCs; blue), revealing 5 distinct clusters. **D.** Heatmap depicting average expression of genes significantly enriched in each cluster (adjusted p-value < 0.05). **E.** UMAP of Sham SCs color-coded by genotype (WT or Sarm1KO). **F.** Bar graph showing the proportion of WT and Sarm1KO Sham SCs in each cluster. **G.** Bar graph illustrating the distribution of clusters within WT and Sarm1KO Sham SC populations. **H.** Volcano plot of differentially expressed genes between WT and Sarm1KO in pseudo-bulk samples of Sham SCs. X-axis represents log2 fold change, Y-axis represents -log10 p-value. Black dots above the line indicate significantly differentially expressed genes (adjusted p<0.05). Only 12 genes met this significance threshold, highlighting the overall similarity in gene expression between WT and Sarm1KO Sham SCs.

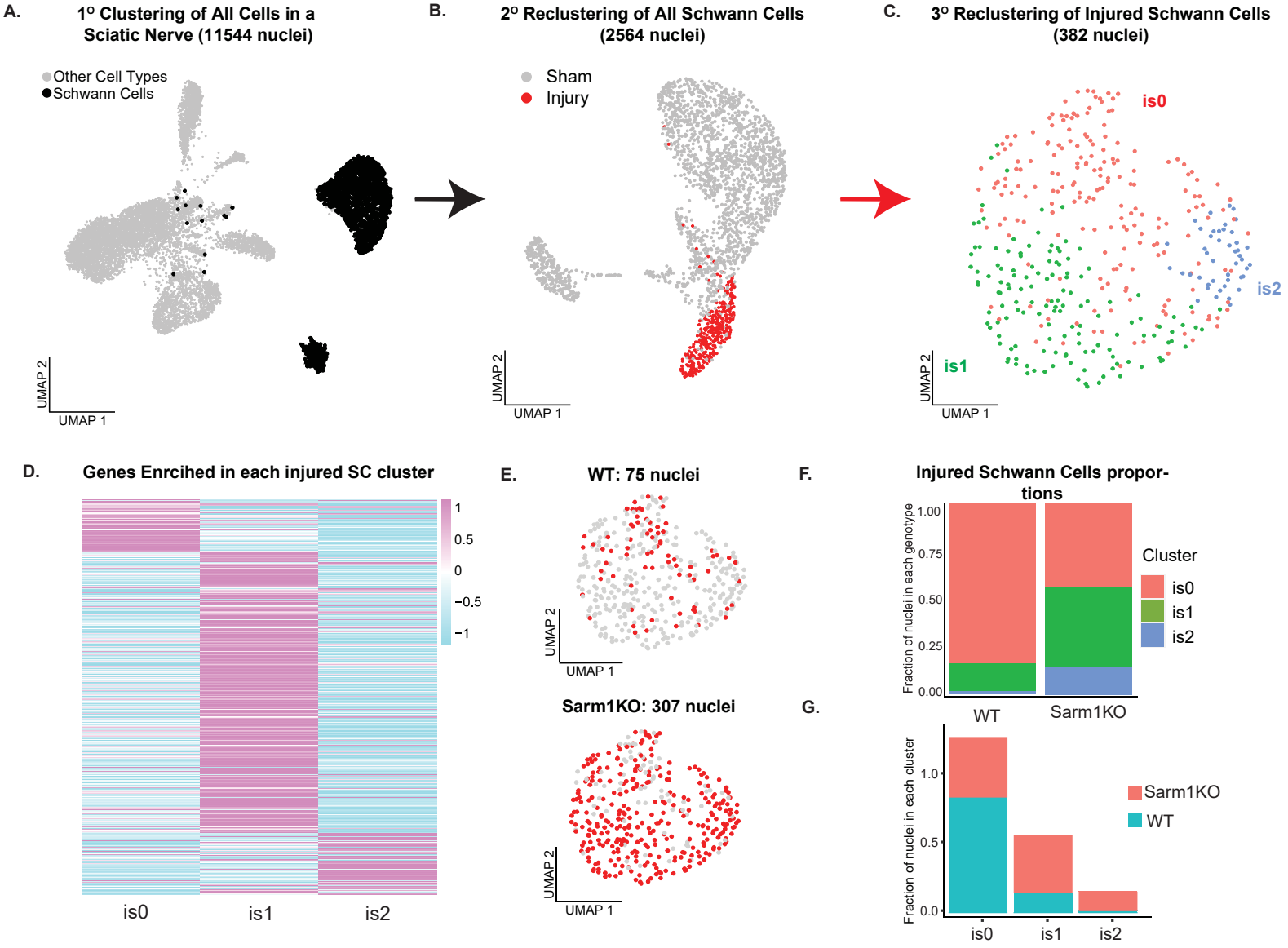

Figure 3. Schwann Cells 1 day after injury across WT and Sarm1KO sciatic nerves

Figure 3: Transcriptional profiling of Schwann Cells one day post-injury in WT and Sarm1KO sciatic nerves. A. UMAP highlighting Schwann Cell (SC) clusters a1 and a6 (in black) selected for reclustering analysis. **B.** UMAP of reclustered SCs, with nuclei from injured nerves (Injured SCs) highlighted in red. **C.** UMAP showing reclustering results of Injured SCs only, revealing three distinct clusters: is0, is1, and is2. **D.** Heatmap displaying genes with significant differential expression between Injured SC clusters (adjusted p-value < 0.05). **E.** Bar graph illustrating the proportion of WT and Sarm1KO cells within each Injured SC cluster. **F.** Bar graph showing the distribution of Injured SC clusters within WT and Sarm1KO genotypes.

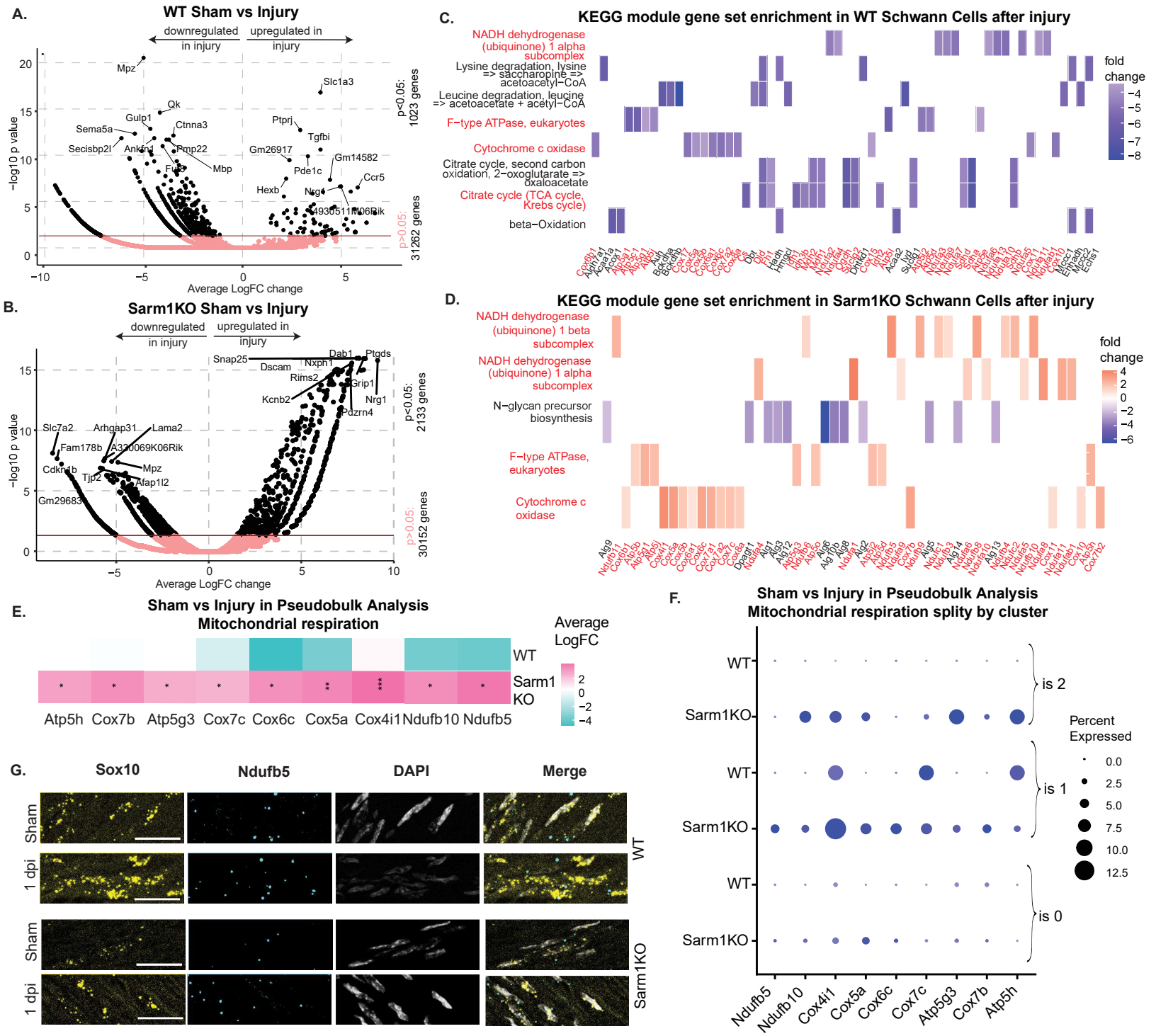

Figure 4. Sarm1KO Schwann Cells 1 day post injury upregulate mitochondrial respiration genes

Figure 4: Sarm1KO Schwann Cells upregulate mitochondrial respiration genes one day post-injury. A-B. Violin plots depicting differentially expressed genes in response to injury, as revealed by pseudo-bulk analysis in (A) WT and (B) Sarm1KO Schwann Cells. **C-D.** Heatmaps showing KEGG module gene set enrichment in (C) WT and (D) Sarm1KO Schwann Cells after injury. **E.** Bar graph of manually selected mitochondrial respiration genes identified from KEGG analysis (C-D), plotted based on pseudo-bulk analysis. *$p<0.05$, **$p<0.01$, ***$p<0.001$. **F.** Dot plot showing expression of genes significantly regulated in response to injury (as identified in C and D), split by genotype and cluster. Note the enrichment of these genes in clusters is1 and is2, particularly in Sarm1KO Schwann Cells. **G.** Representative images of in situ hybridization for Ndufb5 (mitochondrial respiration gene) and Sox10 (Schwann Cell marker) in WT and Sarm1KO sciatic nerves under sham conditions and 1 day post-injury. Scale bar: 100 µm.

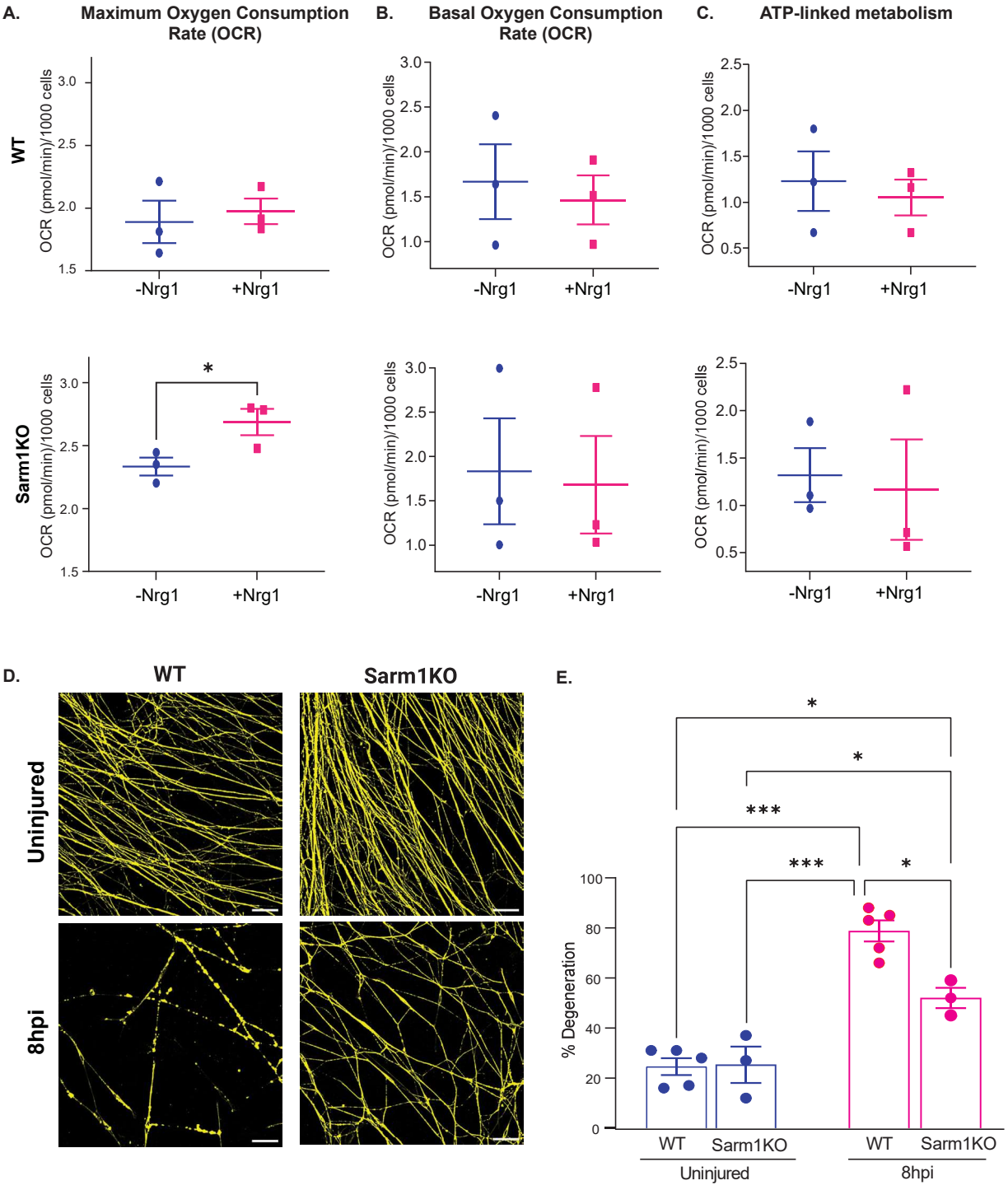

Figure 5: Sarm1KO Schwann Cells upreglate mitochondrial respiration after injury and are protective against axon degenerationin *in vitro*

Figure 5: Sarm1KO Schwann Cells exhibit increased mitochondrial respiration after injury and provide enhanced protection against axon degeneration in vitro. A-C. Oxygen Consumption Rate (OCR) measurements in primary mouse Schwann Cells from WT or Sarm1KO backgrounds using Seahorse XFe96 analyzer: **A.** Maximum OCR **B.** Basal OCR **C.** ATP-linked OCR. Each data point represents the mean of technical replicates from one mouse litter. Unpaired two-tailed t-test was used to analyze differences between conditions (± Neuregulin 1). *$p = 0.0486$ **D.** Representative images of Superior Cervical Ganglia co-cultured with either WT or Sarm1KO Schwann Cells, under uninjured conditions or 8 hours post-injury (hpi). Axons visualized by Tuj1 antibody staining. Scale bar = 50 µm. **E.** Quantification of axon degeneration from images in (D), performed by an investigator blinded to experimental conditions. Each data point represents the average of technical replicates from one mouse litter. Two-way ANOVA with Tukey's multiple comparison test was performed. *$p < 0.05$, ***$p < 0.001$.

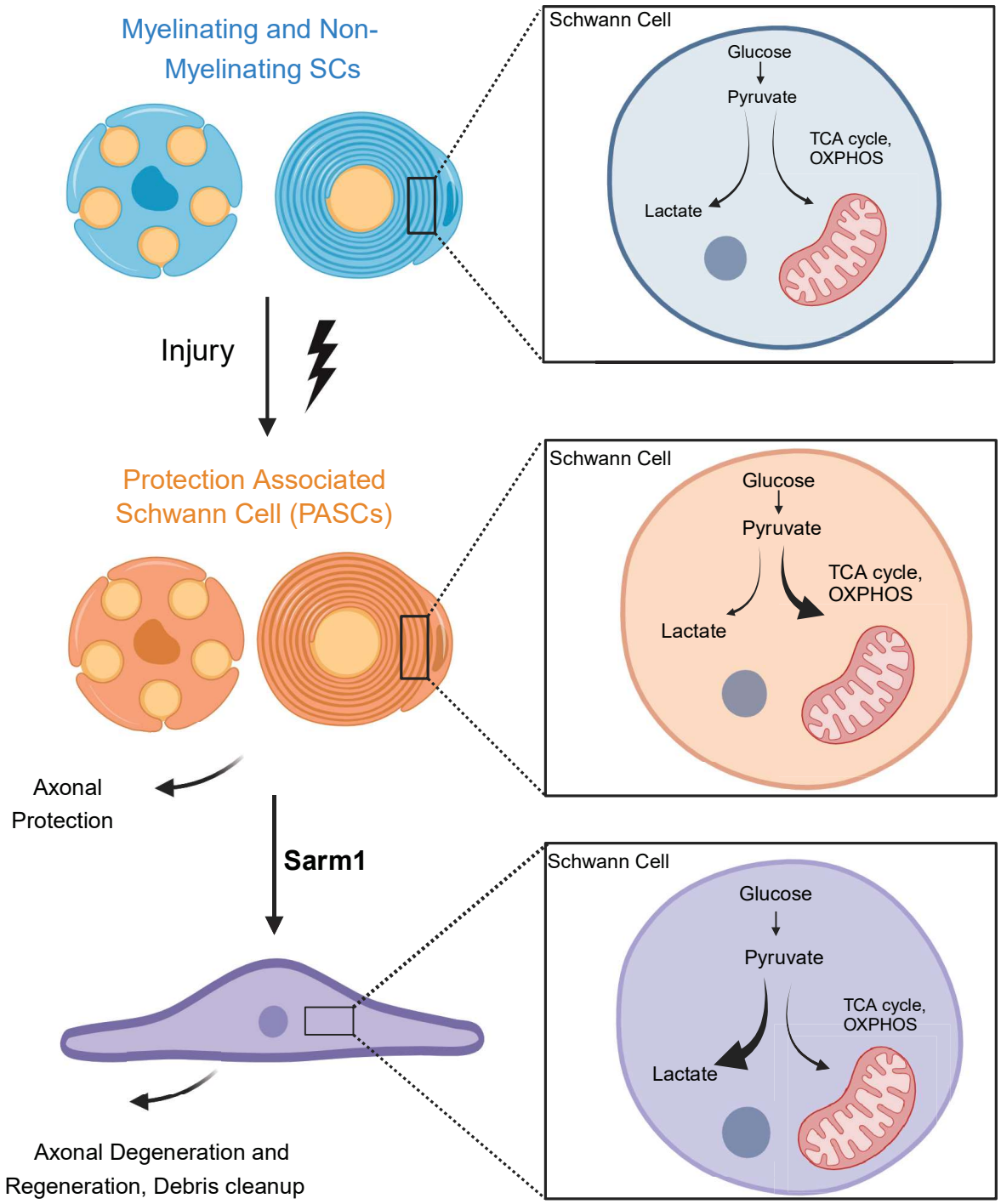

Figure 6. Proposed Role of Sarm1 in Schwann Cells after axon injury

Figure 6. Proposed Role of Sarm1 in Schwann Cell Metabolic Reprogramming After Axon Injury. Schematic representation of SC metabolic states before and after axon injury: **1.** Pre-injury: Myelinating and non-myelinating SCs maintain a balance between glycolysis and mitochondrial respiration (TCA cycle, OXPHOS). **2.** Early post-injury: SCs transition to PASCs, characterized by increased mitochondrial respiration and reduced lactate production. This metabolic state promotes axonal protection. **3.** Late post-injury: Sarm1 activation triggers a metabolic shift towards increased glycolysis and lactate production, with reduced mitochondrial respiration. This state supports axonal degeneration, regeneration, and debris cleanup. Each stage is illustrated with both a cross-sectional view of the nerve (left) and a detailed metabolic diagram of a single SC (right). Arrows indicate the relative flux through different metabolic pathways, with thicker arrows representing increased activity.

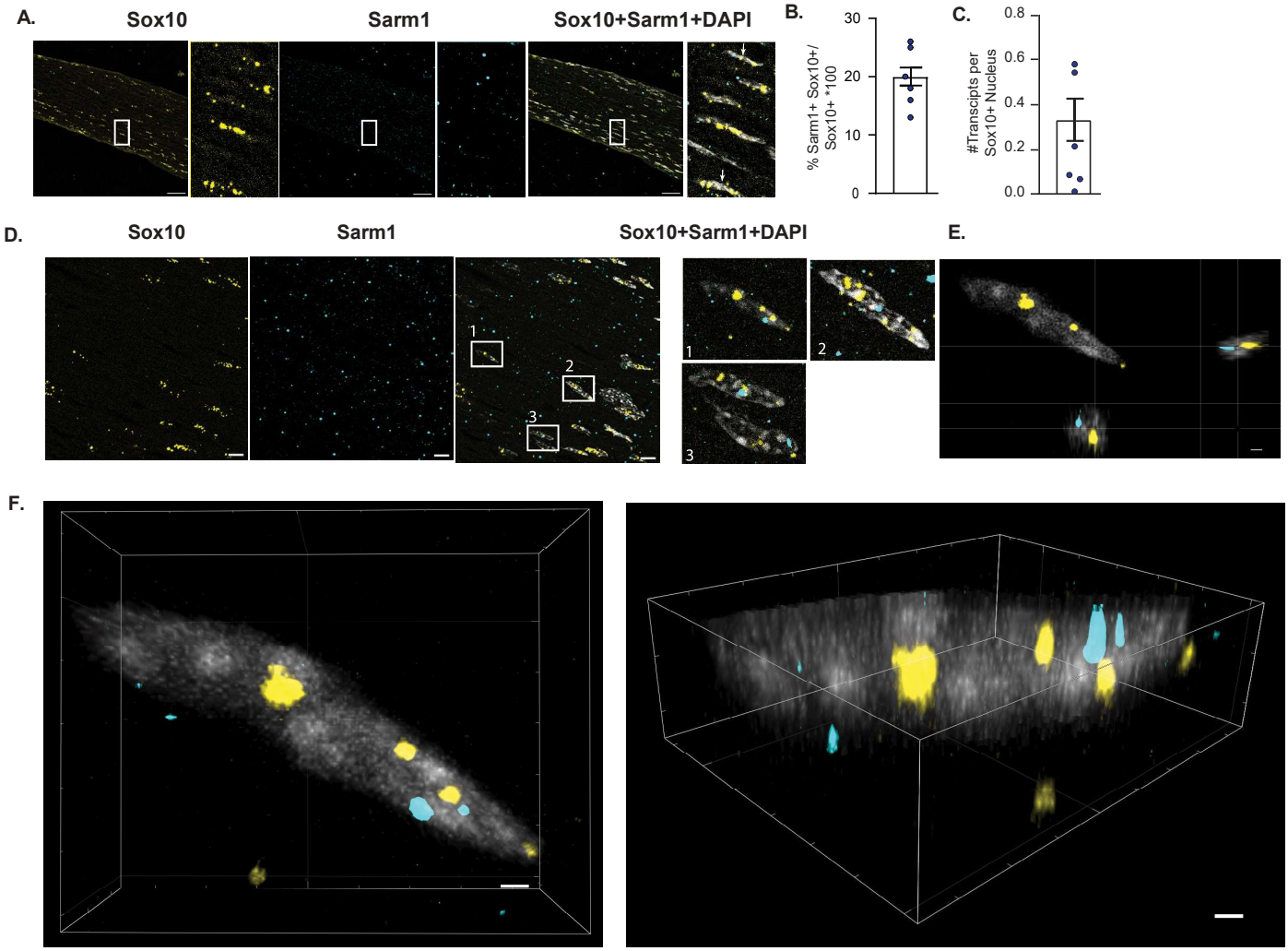

Supplemental Figure 1.1: Sarm1 mRNA Expression in Sox10-Positive Schwann Cells

Supplemental Figure 1.1: Sarm1 mRNA Expression in Sox10-Positive Schwann Cells. A. Representative images of in situ hybridization targeting Sox10 (yellow) and Sarm1 (cyan) RNA transcripts in sham and 1 day post-injury (dpi) sciatic nerves. Merged images include DAPI (gray). Scale bar = 50 μm. Insets show higher magnification of boxed areas. **B.** Quantification of the percentage of Sox10+ nuclei that are also Sarm1+ (B) and the average number of Sarm1 transcripts per Sox10+ nucleus (C). Data presented as mean ± SEM. **D.** Higher magnification images of in situ hybridization for Sox10, Sarm1, and merged with DAPI in sham sciatic nerves. Scale bar = 10 μm. Numbered boxes indicate regions shown in higher magnification insets. **D.** High magnification image showing co-localization of Sox10 and Sarm1 transcripts within individual nuclei. **E.** 3D reconstructions of SC nucleus showing the spatial relationship between Sox10 (yellow) and Sarm1 (cyan) transcripts. Left: perspective view. Right: cross-sectional view. Scale bar = 1 μm.

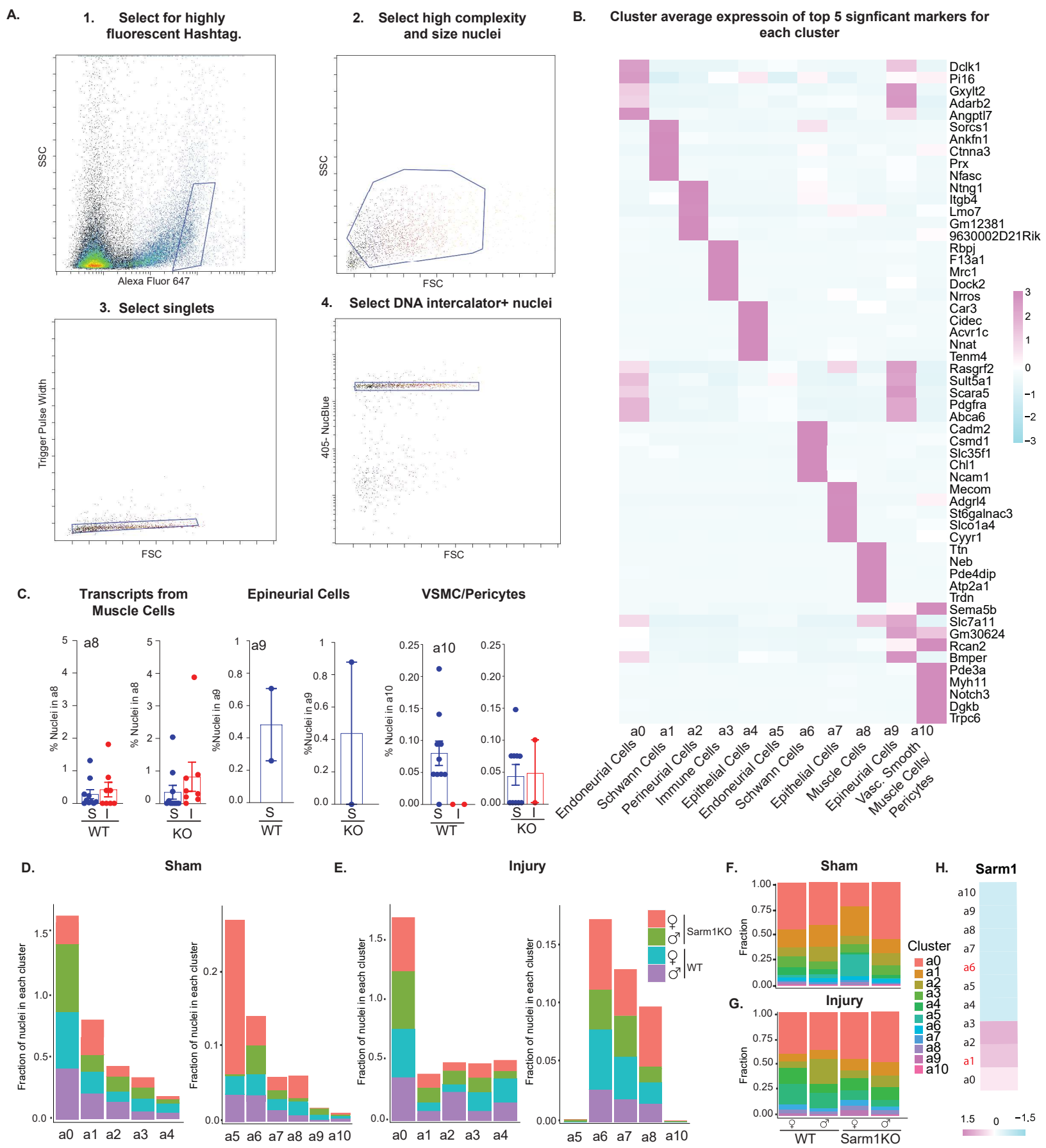

Supplemental Figure 1.2: Supplemental Information on Single-Nucleus RNA Sequencing Analysis

Supplemental Figure 1.2: Supplemental Information on Single-Nucleus RNA Sequencing Analysis. A. Fluorescence-activated cell sorting (FACS) workflow for nuclei selection: 1)Selection of nuclei with high fluorescence for nuclear pore complex antibodies; 2) Gating for high complexity (SSC) and size (FSC) nuclei; 3) Selection of singlets; 4) Gating for DNA intercalator-positive nuclei. **B.** Heatmap showing cluster-level expression of top 5 marker genes for each identified cluster, based on relative expression levels. **C.** Bar plots depicting the percentage of nuclei in each cluster for transcripts from muscle cells, epineurial cells, and vascular smooth muscle cells (VSMC)/pericytes, relative to each experimental condition. **D-E.** Stacked bar plots showing the proportion of nuclei from each cluster in sham (D) and injured (E) conditions, split by experimental group (WT, Sarm1KO) and sex (male, female). **F-G.** Stacked bar plots illustrating the proportion of nuclei from each cluster by genotype (WT, Sarm1KO) and sex for sham (F) and injured (G) Schwann cells. **H.** Heatmap showing Sarm1 expression across clusters in WT sham and injured cells.

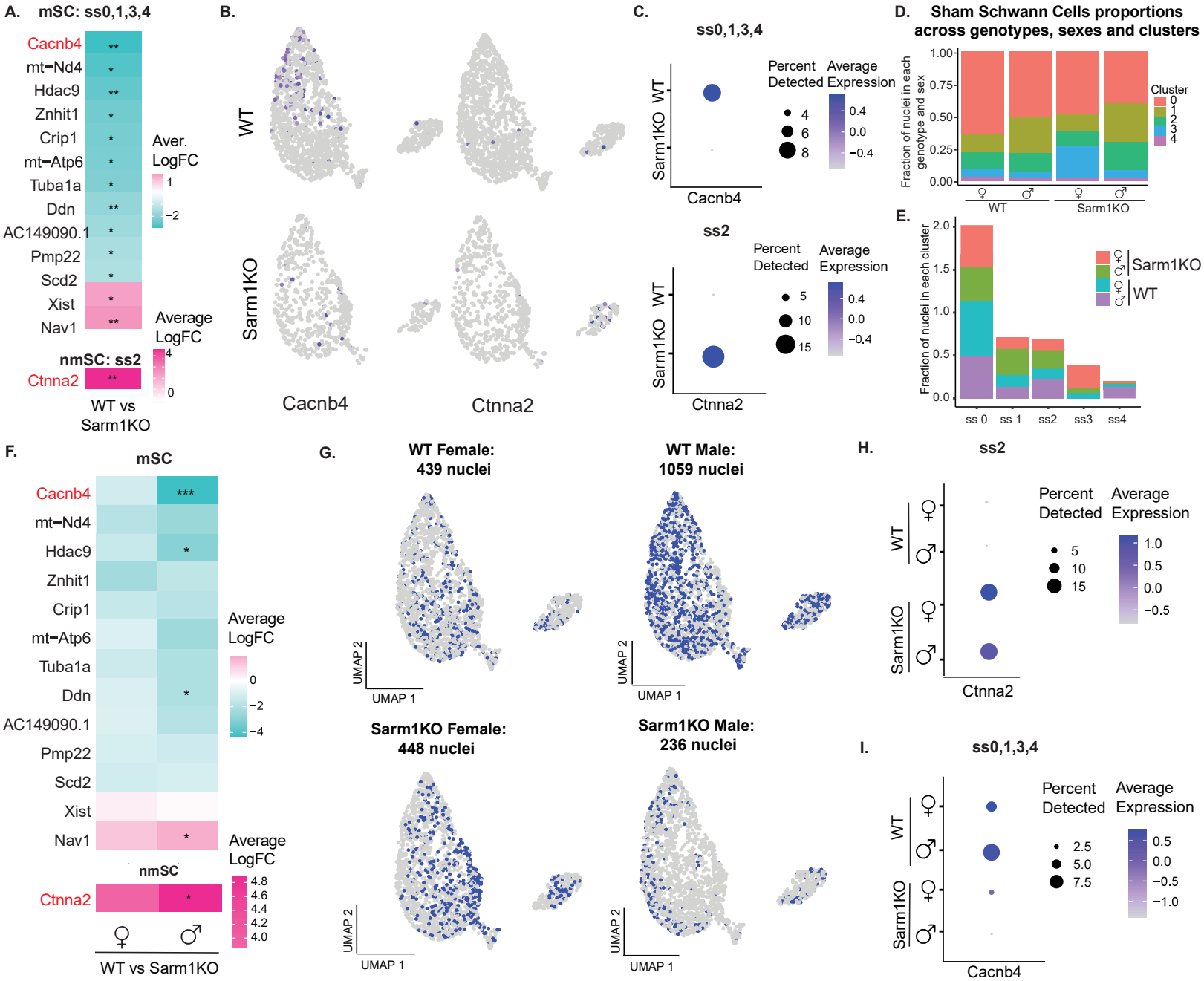

Supplemental Figure 2: Supplemental Analysis of Differential Gene Expression in Sham Schwann Cells

Supplemental Figure 2: Supplemental Analysis of Differential Gene Expression in Sham Schwann Cells. A. Heatmap displaying top differentially expressed genes between WT and Sarm1KO sham Schwann cells (SCs), based on pseudo-bulk analysis. Color intensity indicates average log fold change. * $p<0.05$; ** $p<0.01$; *** $p<0.001$. **B.** UMAP feature plots showing expression of Cacnb4 (downregulated) and Ctnna2 (upregulated) in WT and Sarm1KO sham SCs. **C.** Dot plots quantifying expression of Cacnb4 and Ctnna2 in clusters ss0,1,3,4 and ss2, respectively. Dot size represents percent of cells expressing the gene, while color intensity indicates average expression level. **D.** Stacked bar plot showing the proportion of sham SCs in each cluster, split by genotype (WT, Sarm1KO) and sex. **E.** Stacked bar plot depicting the distribution of clusters within each experimental condition (WT and Sarm1KO, male and female) for sham SCs. **F.** Heatmap of differentially expressed genes between WT and Sarm1KO sham SCs, split by sex. **G.** UMAP plots showing distribution of WT and Sarm1KO male and female nuclei across identified clusters. **H-I.** Dot plots visualizing expression of Ctnna2 and Cacnb4 in sham SCs, split by genotype and sex for (H) cluster ss2 and (I) clusters ss0, ss1, ss3, and ss4.

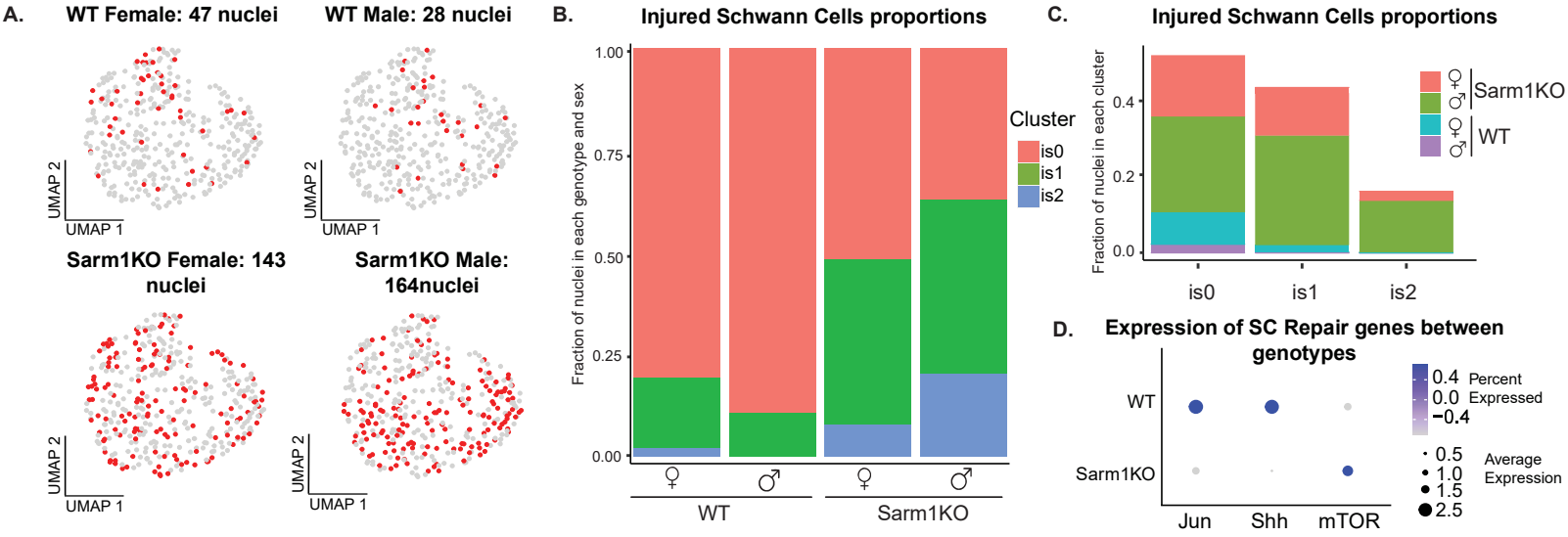

Supplemental Figure 3: Supplemental Analysis of Injured Schwann Cells in WT and Sarm1KO Mice

Supplemental Figure 3: Supplemental Analysis of Injured Schwann Cells in WT and Sarm1KO Mice. A. UMAP plots showing distribution of injured Schwann cells (SCs), split by genotype (WT or Sarm1KO) and sex. Red cells indicate the selected SCs for indicated genotype and sex, while gray indicates all the injured SCs. Total nuclei counts are indicated for each condition. **B.** Stacked bar plot illustrating the proportion of injured SCs in each cluster (is0, is1, is2), stratified by genotype and sex. **C.** Bar plot depicting the proportion of injured SCs from each experimental condition (WT and Sarm1KO, male and female) within each cluster (is0, is1, is2). **D.** Dot plot showing expression levels of SC repair genes (Jun, Shh, mTOR) in WT and Sarm1KO injured SCs. Dot size represents the percentage of cells expressing the gene, while color intensity indicates average expression level.

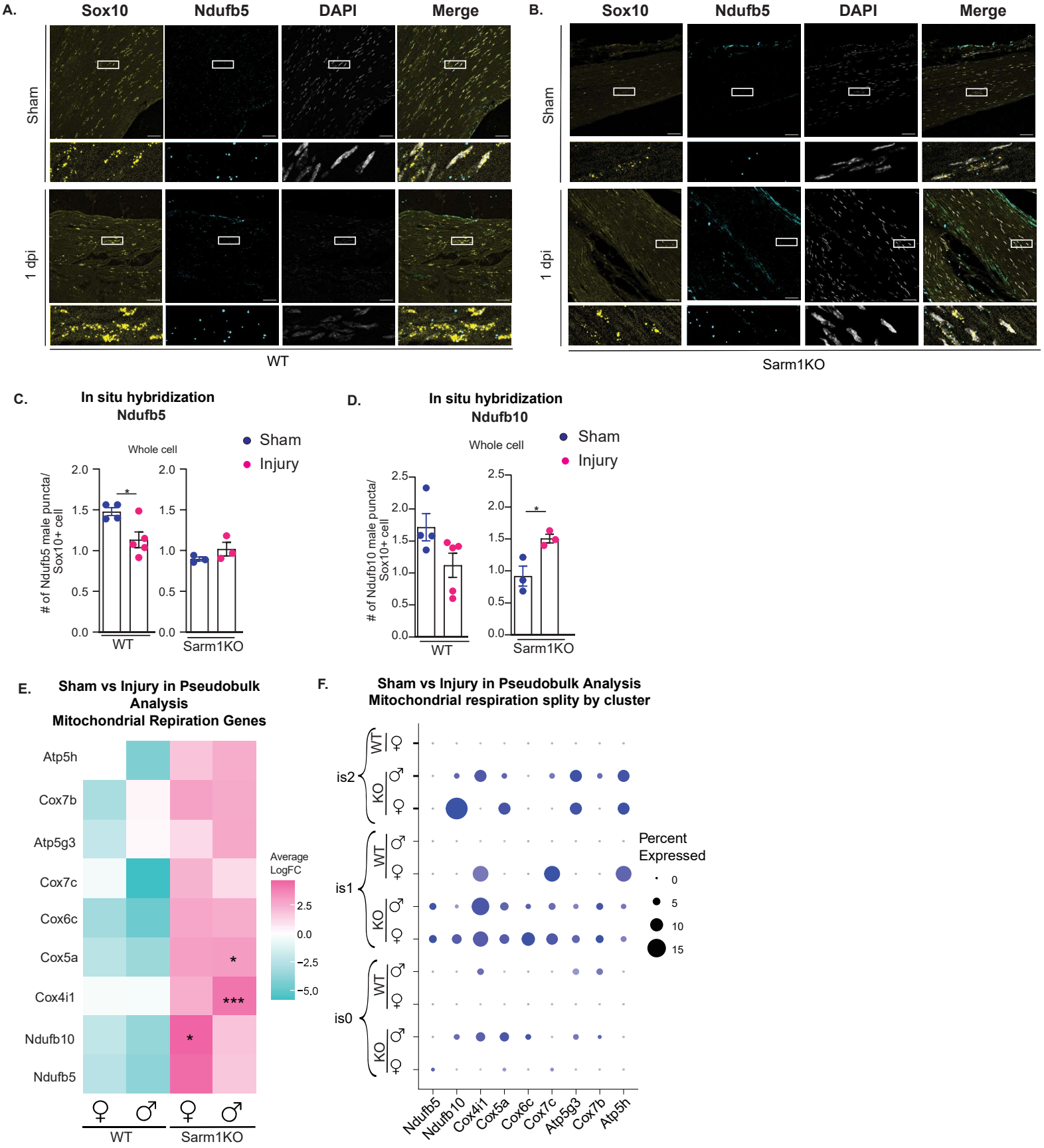

Supplemental Figure 4: Analysis of mitochondrial gene expression in wild-type and Sarm1KO Schwann cells after nerve injury.

Supplemental Figure 4: Analysis of mitochondrial gene expression in wild-type and Sarm1KO Schwann cells after nerve injury. A-B. Representative images of in situ hybridization for Ndufb5 (cyan) and Sox10 (yellow) in sciatic nerves from (A) wild-type (WT) and (B) Sarm1 knockout (Sarm1KO) mice under sham conditions and 1 day post-injury (1 dpi). Lower panels show magnified views of the boxed regions. DAPI nuclear staining shown in white. Scale bar = 50 µm. **C-D.** Quantification of (C) Ndufb5 and (D) Ndufb10 transcript numbers in Sox10-positive cells from WT and Sarm1KO sciatic nerves under sham and injury conditions. Data shown as mean ± SEM. * $p = 0.0213$ for Ndufb5 (C), * $p = 0.0256$ for Ndufb10 (D). **E.** Heatmap showing log fold changes in expression of mitochondrial respiration genes between sham and injured conditions in SCs, based on pseudo bulk sc-RNA-seq analysis. Data are split by sex and genotype (WT vs Sarm1KO). Color scale indicates magnitude and direction of change. **F.** Dot plot depicting expression of selected mitochondrial respiration genes across different Schwann cell clusters (is0, is1, is2) in WT and Sarm1KO conditions. Dot size represents percentage of cells expressing the gene, while color intensity indicates average expression level.

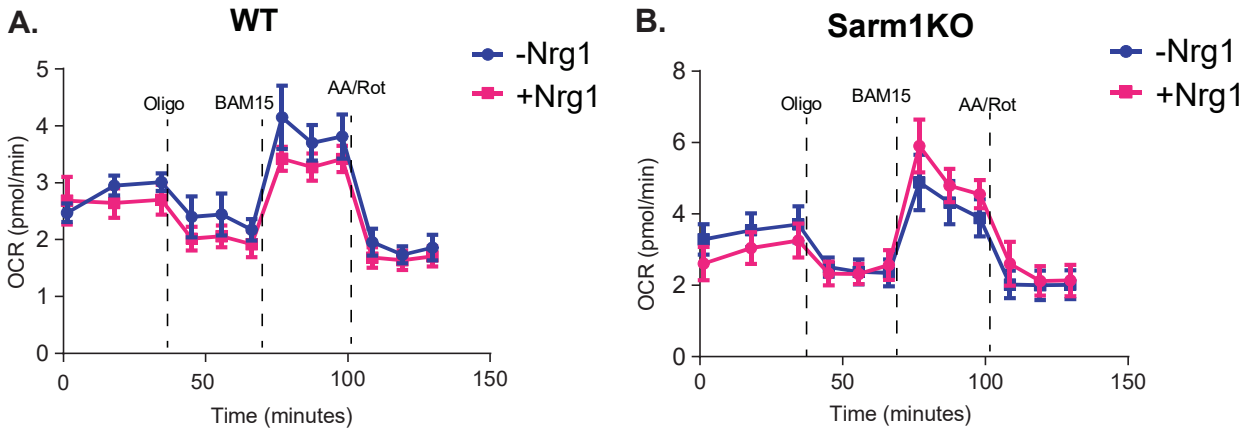

Supplemental Figure 5. Oxygen consumption rates in wild-type and Sarm1KO Schwann cells.

Supplemental Figure 5. Oxygen consumption rates in wild-type and Sarm1KO Schwann cells. A-B. Representative traces showing oxygen consumption rates (OCR) in (A) wild-type (WT) and (B) Sarm1 knockout (Sarm1KO) Schwann cells during a mitochondrial stress test. Cells were treated with or without Neuregulin1 (Nrg1) to mimic injury conditions. OCR was measured at baseline and following sequential addition of oligomycin (Oligo), BAM15, and a combination of antimycin A and rotenone (AA/Rot) as indicated by vertical dashed lines. Data points represent mean ± standard error of the mean (SEM) from technical replicates. Blue lines: control (-Nrg1); Pink lines: Nrg1-treated (+Nrg1).